UC San Diego
UC San Diego Previously Published Works

Title
Marine Fog: Challenges and Advancements in Observations, Modeling, and Forecasting Introduction

Permalink
https://escholarship.org/uc/item/4rp873k2

ISBN
978-3-319-45227-2

Authors
Koracin, Darko
Dorman, Clive E

Publication Date
2017

DOI
10.1007/978-3-319-45229-6_1

Peer reviewed

RESEARCH ARTICLE

World marine fog analysis based on 58-years of ship observations

Clive E. Dorman[1,2] 🔘 | John Mejia[3] 🔘 | Darko Koračin[3,4] | Daniel McEvoy[3,5]

[1]Integrative Oceanography Division, Scripps Institution of Oceanography, University of California, San Diego, La Jolla, California

[2]Department of Geological Sciences, San Diego State University, San Diego, California

[3]Department of Atmospheric Sciences, Desert Research Institute, Reno, Nevada

[4]Physics Department, Faculty of Science, University of Split, Split, Croatia

[5]Western Regional Climate Center, Desert Research Institute, Reno, Nevada

Correspondence
Clive E. Dorman, Integrative Oceanography Division, Scripps Institution of Oceanography, La Jolla, CA 92093-0209.
Email: cdorman@ucsd.edu

Funding information
Croatian Science Foundation, Grant/Award Numbers: IP-06-2016-1955, IP-2014-09-3606; Desert Research Institute (DRI) and its Division of Atmospheric Sciences; Office Of Naval Research, Grant/Award Number: N00014-18-1-2472; European Union through the European Regional Development Fund, Grant/Award Number: KK.01.1.1.01.0003

Abstract

This study presents the first global-scale comprehensive climatology of marine fog and is based on ICOADS ship present weather observations for the period 1950–2007. In general, the median marine fog occurrence away from the polar oceans is low (0.2%). Substantially greater marine fog occurrences are limited to four regions, not including the polar region. Fog occurrence maxima along the western side of the sub-polar ocean gyre occur during the warm season and over the shelf, which includes one centred over the Northwest Pacific Kuril Islands (60%) and one over the Northwest Atlantic Grand Banks (45%), while a third lies over the Argentinean shelf break. Fog maxima over seven marginal seas occur over the Okhotsk Sea, Sea of Japan, Yellow Sea, South China Sea, Nova Scotia, North Sea, and Baltic Sea. Five wind-driven coastal upwelling zone maxima comprise the California-Oregon, Namibia-South Africa, Peru, Morocco and Arabian regions. Maximum upwelling fog occurrence during the warm season was found to be inversely proportional to the minimum sea surface temperature (SST). Most fog maximum occurrence locations lie over SST minima in shallow water during the warm season and are capped by a stable lower atmosphere. Positive correlations (up to 0.79) were found between 5-year moving averages of fog in the Kuril Islands and the North Pacific Oscillation. Five-year moving averages of fog in the Grand Banks were positively and significantly correlated (up to 0.56), with the North Atlantic Oscillation represented by the sea level pressure difference between Gibraltar and Reykjavik. In contrast, 5-year moving averages of fog in the Grand Banks and the Atlantic Multidecadal Oscillation index were negatively and significantly correlated (up to −0.75).

KEYWORDS
Atlantic ocean, climate index, climate variability, fog, Indian ocean, Pacific ocean, SST, upwelling

1 | INTRODUCTION

The first major marine fog investigation was conducted by Taylor (1917) using ship iceberg patrols to make the first ground breaking weather measurements in sea fog. The only worldwide marine fog analysis that was found was a subjective, hand-drawn analysis (U.S. Department of Agriculture, 1938). Marine fog field work in California and Great Britain expanded after World War II (WWII), attempting to discover key relationships by focused studies (Lewis *et al.*, 2004). With more observations and a better understanding of weather conditions, basic work on the dynamics of fog formation began to emerge (Wang, 1985). Improved technology allowed micro-scale measurements to illuminate missing portions of fog dynamics, especially over land (Gultepe *et al.*, 2007). Eastman *et al.* (2011; 2014) presented sea fog occurrences

and trends based on $5° \times 5°$ and $10° \times 10°$ latitude–longitude areas over portions of the oceans, finding that there was a strong negative correlation of stratus and stratocumulus clouds with SST in eastern subtropical oceans. A worldwide summary of ocean fog research was presented in Koračin et al. (2014) and expanded upon by Koračin et al. (2017).

This paper further discusses the highlights of Dorman et al. (2017), with the first published quantitative analysis of marine fog for the non-polar world. Here, we first describe the ship observations used and the methods for applying the data to our global study. It should be noted that for the non-polar world, marine fog is infrequent, with high frequency occurrences concentrated in 17 locations. In this review, these locations are organized into four areas with common aspects to explore their significant features. Two of the locations have sufficient observations to support a trend analysis and comparison with oceanic circulation indices.

2 | METHODS

2.1 | Data

This study uses the International Comprehensive Ocean–Atmosphere Data Set (ICOADS) marine data for 1950–2007 (Freeman et al., 2016) to retrieve the present weather code, which characterizes weather at the time of observation. Fog data are based upon the present weather portion of the synoptic weather code or SYNOP (WMO, 2009). This is an observer's subjective weather assessment, with a two-digit code from 01 to 99 based on SYNOP rules. Marine fog is defined as a cloud touching the ocean surface that is deeper than 10 m, with a horizontal visibility less than 1 km. Shallow fog and mist are distinctly different (Woodruff et al., 1987; Worley et al., 2005). International acceptance of a uniform weather observation code and a dramatic increase in ship reports after WWII greatly improved the quantity and quality of ocean weather records.

The ICOADS present weather observations from 1950 to 2007 were organized into seasons (June–August [JJA], September–November [SON], December–February [DJF], and March–May [MAM]) and one-degree latitude-longitude grid bins over the non-polar global oceans. The centre of the bin represents a whole degree of the latitude and longitude intersection. The average percent of fog occurrence was computed by the sum of fog observations divided by the total number of seasonal present weather observations for a grid bin and multiplied by 100.

2.2 | Number of observations

We investigated how the number of observations affects the occurrence computation by comparing surrounding grid bins in different areas (Dorman et al., 2017). Fog percent occurrence versus observation number has the greatest variation, with a number of observations <20, and decreases as the number of observations increases. In addition, there are occasional erratic fog occurrences when the number of observations is less than 100, which can be greater than 10 times the surrounding grid bin values. These occurrences were eliminated by establishing a minimum seasonal threshold of 100 observations in a grid bin.

There is no significant relationship between fog occurrence and the number of observations in data-rich areas. A representative example is the bounding box 44°–47°N, 51°–48°W, for which occurrences were computed in each of the 16 grid bins for each JJA season from 1950 to 2007, resulting in 928 data points, with a standard deviation of 14%. The correlation coefficient between occurrence and number of observations is 0.13, indicating that they are poorly related.

An analysis was performed on the diurnal variation in the number ship observations and the number of fog observations over the representative area 43°–48°N, 42°–53°W for JJA for the period of record. Although the number of observations and the number of fog observations was greater during night than those during the day, the differences for both are not significant, as the differences were less than their respective standard deviations.

The number of ship observations in JJA per degree grid bin for 1950–2007 (Figure 1a) is similar to that in the other seasons. Ship observations are too sparse for analysis in polar regions and large portions south of the equator.

To examine the interannual and decadal variations in fog, we first remove the long-term linear trend, which has been argued to have limitations in studies of ICOADS data (Norris, 1999; Eastman et al., 2011). To partly avoid such limitations, we perform temporal variability analyses only over locations with the greatest frequency and largest number of observations and signal-to-noise ratios: the Kuril Islands (KI) and Grand Banks (GB). The linear trend is then removed using a linear least-square fit of the data. We then relate the detrended fog data to well-known climate indices. The relationship between the detrended fog time series and detrended climate indices was estimated using Pearson, Spearman and Kendall correlation coefficients. The Pearson correlation coefficient measures the linear relationship between two datasets and assumes that each dataset is normally distributed. The Spearman correlation is a nonparametric measure of the monotonicity of the relationship between two datasets. Unlike the Pearson correlation, the Spearman correlation does not assume that both datasets are normally distributed. Pearson and Spearman correlation coefficients close to 1 and −1 suggest a linear relationship and an exact monotonic relationship, respectively. The
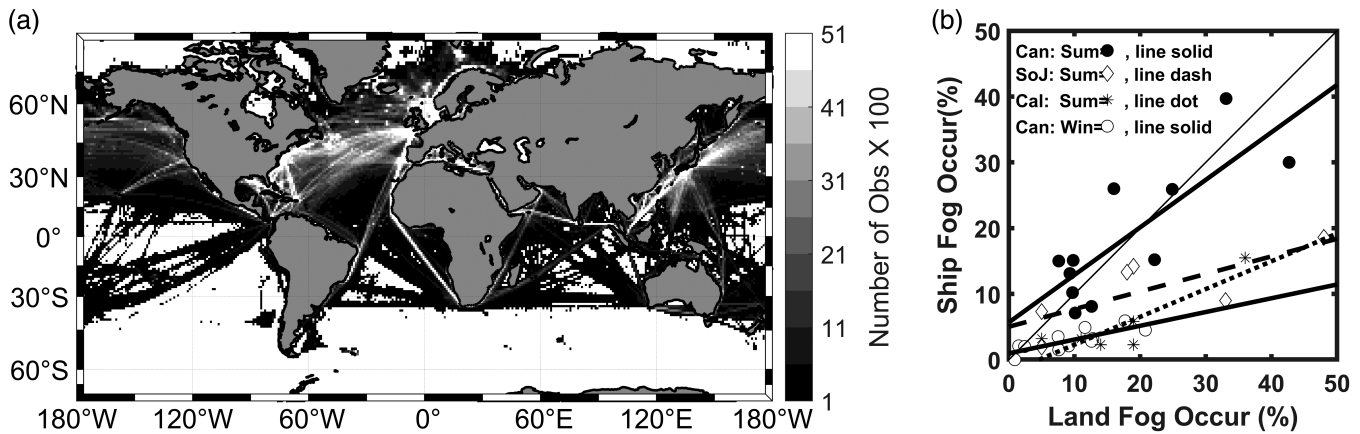
FIGURE 1 (a) JJA number of ICOADS present weather observations greater than 100 per 1° grid bin for 1950–2007. Greatest numbers are along major ship tracks in northern oceans. (b) Land station and ship observed summer fog occurrences for eastern Canada (Can), the Sea of Japan (SoJ) and California (Cal). The winter fog occurrences are only shown for eastern Canada as they are irregular and poorly correlated in the winter for the Sea of Japan and California (Table 1). Thin diagonal line is the 1:1 ratio of ship to land occurrences for reference

Kendall coefficient is a measure of the rank correlation. Values close to 1 indicate strong agreement, and values close to −1 indicate strong disagreement. We performed these statistics using yearly data to assess relationships within the interannual variations and 5-year running means to assess the lower frequency modes of the variations.

3 | COMPARISON WITH OTHER FOG OBSERVATIONS

Ship fog reports are consistent with other observations. At the high occurrence extreme are weather forecasters for the Hibernia oil platform on the GB, who reported a maximum fog occurrence of 50% in August (Isaac, 2015), whereas the nearest grid bin JJA ship-based value is 40%. In a model-based analysis of GB fog, Bassem (2015) estimated July fog frequency at 46.75°N, 48.5°W as 57% (JJA ship is 34%) and December fog frequency as 12% (DJF ship-based value is 7%).

Comparisons of the nearest ship value with coastal stations in several different geographic locations show that most ship-based fog values are either similar or less than land fog values (Dorman *et al.*, 2017). The relationship between land and ship results is most apparent when stations are subdivided in a local, climatically similar area and by season. Fortunately, there are three such areas where ship and coastal measurements are available that are readily comparable to ship measurements: eastern Canada (Wang, 2006), Sea of Japan (Dashko and Yudin, 1998; Dashko and Varlamov, 2003) and California (Dorman *et al.* (2017)). The statistics for areas and seasons results in high positive correlation coefficients (0.76–0.87) for all summers and eastern Canada winter (Table 1). The summer fitted line for each area has a positive slope and all summer fitted lines are offset above those for winter (Figure 1b). In contrast, the Sea of Japan and California winter land-ship comparisons are uneven and without a linear relationship due to low, irregularly distributed occurrences, especially over water. If not partitioned by local area and season, ship and land fog occurrences are poorly correlated.

TABLE 1 Relationship between land station and ship observed fog occurrence

| Season | Area | # pts | Mean (%) | | | Fitted line coef. | |
			Land	Ship	Corr	Slope	Zero cross
JJA	**E. Canada**	11	18.0	18.7	**0.80**	0.72	5.67
	Sea Japan	6	21.3	10.7	**0.76**	0.27	5.02
	California	6	17.3	5.4	**0.87**	0.42	−1.94
DJF	**E. Canada**	11	9.5	3.0	**0.80**	0.21	0.97
	Sea Japan	6	1.3	0.9	−0.37	−0.13	1.08
	California	6	11.3	4.0	0.00	0.00	4.00

Note: Bold face indicates high correlation coefficients and good line fits.

Satellites detect low cloud and fog (SLC&F) mixed together without distinguishing them. Distribution of SLC&F for June–September along California-Oregon coast (Torregrosa *et al.*, 2016) is substantially different from ship-based fog occurrences as expected. Greatest SLC&F occurrence (>50%) and broadest cross-coast section (>400 km) is along 35°N. Occurrence decreases toward north to 33% and narrows to about 100 km along 41°N. In contrast, ship-based fog occurrence maximum extends only 1 or 2 grid points offshore and is situated along coast in a SLC&F moderate occurrence area. Greatest ship occurrence is 16.6% where the SLF&C is 46%. Away from the ship maximum, the SLC&F occurrence is 3–10 times greater. A rather similar SLC&F (Cermak, 2012) and ship-based fog distribution (Dorman *et al.*, 2017) is along the South African coast. However, the satellite observation is at the cloudiest time of day (7 LST(LST+2)), which should be reduced by ~1/3 to compare with 24-hr ship observations (Gultepe *et al.*, 2007). This results in satellite values mostly similar to ship values (within 10%) at the coast over the average of the five highest values in each of two maxima. Away from the maxima, SLF&C values along South Africa are up to 10 times greater. The ICOADS ship-based fog occurrence values are consistent with SLC&F observations as the latter are mostly stratus over water (Combs *et al.*, 2010).

The bulk of land measurements show higher fog occurrences than ship measurements. This is possibly because coastal stations have additional factors affecting fog, such as ground radiation (Koračin *et al.*, 2014) and stratus cloud fog at elevated topography (Schemenauer *et al.*, 1988; Leipper, 1994; Dorman *et al.*, 2017). Finally, we have examined many cases throughout the world and found no clear relationship between coastal land station elevation and fog occurrence over water.

4 | OVERVIEW OF NON-POLAR MARINE FOG

The annual median ship fog occurrence over non-polar oceans is low (only 0.2%). (Dorman *et al.*, 2017). Fog occurrences greater than 10 times the median are concentrated in 16 maxima grouped in four regions (Table 2 and Figure 2a, b). One region is on the western side of three sub-polar ocean gyres and over the ocean shelf (KI, GB, and Argentina). Of the seven marginal seas with significant fog, five are on the western side of Northern Hemisphere oceans (Okhotsk Sea, Sea of Japan, Yellow Sea, South China Sea,

TABLE 2 World marine fog maxima for season with greatest fog value and grouped by setting

| Setting | Area | Season | Highest occurrence | | Mean 5 highest (%) |
			(%)	(°Lat–Lon)	
Polar, West Side of Ocean	Kuril Is.	JJA	59.8	47°N 152°E	58.4
	Grand Bks	JJA	45.0	44°N 49°W	43.4
	Argentina	SON[a]	(17.2) 13.3	(41°S 58°W) 41°S 56°W	(13.0) 11.7
Circumpolar	Scotia Sea	DJF	28.2	60°S 54°W	23.8
Marginal Sea	Okhotsk Sea	JJA	54.6	56°N 146°E	50.8
	Nova Scotia	JJA	47.1	43°N 66°W	41.1
	Japan Sea	JJA	28.1	43°N 135°E	26.9
	Yellow Sea	MAM	18.3	33°N 122°E	15.5
	Baltic Sea	MAM	17.2	61°N 17°E	14.8
	North Sea	MAM	9.7	55°N 5°E	8.3
	S. China Sea	MAM	6.7	20°N 106°E	6.5
Wind Driven Coastal Upwelling	Namibia-S. Africa[b]	MAM	24.8n 22.4s	25°S 15°E 30°S 17°E	13.2n 16.2s
	Calif-Or	JJA	16.6	38°N 123°W	14.4
	Peru	DJF	7.9	14°S 76°W	4.6
	Morocco	JJA	4.7	29°N 11°W	3.2
	Arabia	JJA	3.5	19°N 57°E	1.9

Note: n is north, s is south.

[a]Suspect.

[b]Two centres.

FIGURE 2 (a) World marine fog occurrence maxima during season with greatest value. Areas are west side of the oceans (grey bars on left), Circumpolar Current/Scotia Sea (dark bar), marginal seas maxima (white bars in centre) and wind-driven coastal upwelling maxima (dark bars on right, Namibia-South Africa has two centres). The black line across the bar denotes the mean of the five highest values. For Argentina, the maximum is the top of the black bar, a suspiciously high value. The top of the bar is the next highest value. The second black line on the Argentina bar is the mean of the second through sixth highest values as the highest value is suspect. (b) World marine fog occurrence maxima locations based on ICOADS ship observations for 1950–2007. The Namibia-Southwest Africa maximum has two centres. Numbers are the maximum fog grid bin values. A number in parenthesis indicates that the value is suspect and the second highest value follows. Polar regions are excluded because of a lack of sufficient observations
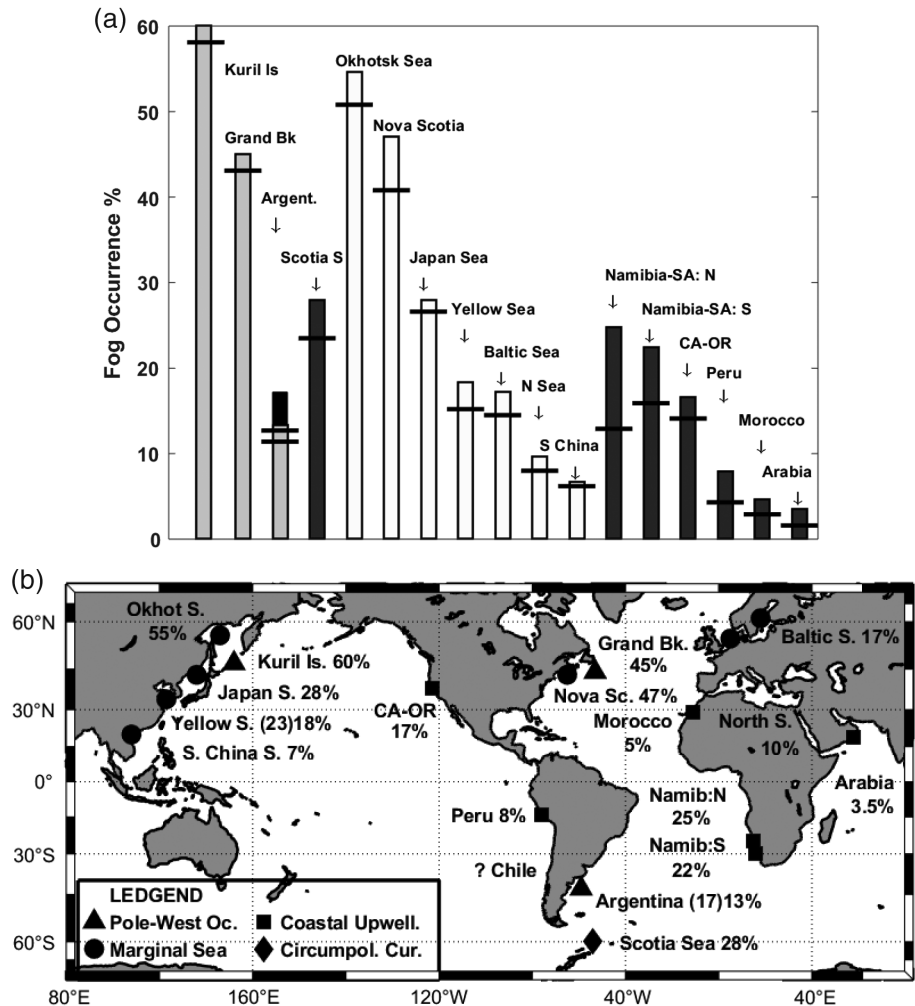
and Nova Scotia), and two are on the eastern side (Baltic Sea and North Sea). Of the five coastal upwelling zone maxima, four are on the eastern side of subtropical ocean gyres (Namibia-South Africa, California-Oregon, Peru, and Morocco), and one is on the northern side of the Indian Ocean (Arabia). All have one centre, except the Namibia-South Africa region, which has two centres. The provisional Scotia Sea maximum in the Circumpolar Ocean is the only deep water fog maximum. However, the polar oceans, which are known for fog, are not examined due to a lack of ship observations.

5 | WEST PACIFIC OCEAN

5.1 | Introduction

A major feature in this section is the Kuril Island-centred maximum extending across the North Pacific in JJA (Table 3). In this section, marginal seas that share some western Pacific atmospheric and oceanographic conditions are included.

5.2 | Kuril Islands

The greatest ship marine fog occurrence is 60%, which occurs over the KI in the Northwest Pacific during JJA (Figure 3 and Table 3). The fog maximum structure is systematic, with the highest values over the central portion of the island chain and surrounded by lower values extending away (Figure 4). Lesser values (40–50%) extend eastward toward 161°E along 46°–49°N. To the northwest, values decrease to a weak minimum and increase irregularly in the Okhotsk Sea, which is treated as a separate feature to be examined in the following section.

The sea surface temperature (SST) isotherm pattern is closely linked with the Northwest Pacific fog distribution, which is centred over the fog maximum in the KI. The large-scale, long-term average Northwest Pacific JJA SSTs are represented by isotherms in Figure 3. The fog occurrence structure conforms to large-scale bends in the 18 and 12°C isotherms. A closed 10°C isotherm extends from Kamchatka to approximately 46°N, 151°E, encompassing the two-thirds of the northern Kuril Island chain and fog centre maximum. Tokinaga and Xie (2009) confirm the 10°C isotherm

TABLE 3 NW Pacific Ocean fog occurrence maxima characteristics

Area	Season	Highest occurrence		Mean 5 highest (%)	Median of sea
		(%)	(°Lat–Lon)		
Kuril Is.	JJA	59.8	47°N 152°E	58.4	—
	SON	19.3	47°N 152°E	15.4	—
	DJF	3.3	48°N 151°E	—	—
	MAM	18.4	44°N 153°E	17.6	—
Okhotsk Sea	JJA	54.6	56°N 146°E	50.8	29.4
	SON	12.7	51°N 143°E	7.7	2.9
		9.1	59°N 153°E	7.9	
	DJF	7.1	52°N 145°E	6.2	1.7
	MAM	47.7	57°N 145°E	39.5	11.4
Sea of Japan	JJA	28.1	43°N 135°E	26.9	9.7
	SON	4.3	42°N 132°E	3.0	0.4
	DJF	2.3	44°N 135°E	2.0	0.5
	MAM	15.5	43°N 136°E	14.7	4.9
Yellow Sea	JJA	(22.8) 14.8	36°N 120°E 37°N 123°E	14.4	8.8
	SON	2.3	38°N 123°E	1.8	0.5
	DJF	4.8	36°N 121°E	4.1	1.3
	MAM	18.3	33°N 122°E	15.5	9.1
South China Sea	JJA	—	—	—	0.0
	SON	—	—	—	0.0
	DJF	5.6	20°N 106°E	4.4	0.1
	MAM	6.7	20°N 106°E	6.5	0.2

Note: The Okhotsk Sea has an irregular distribution with isolated maxima in SON, so the two highest values are shown. Brackets denote a suspicious value. Area for medians: Okhotsk Sea 51°–62°N 138°–156°E, Japan Sea 36°–50°N, 128°–140°E, Yellow Sea 32°–40°N 119°–126°E, South China Sea 16°–24°N 106°–120°E.
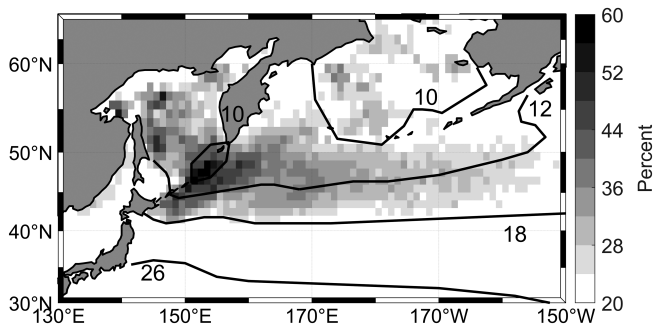

FIGURE 3 N. Pacific JJA ICOADS percent of fog observations at grid bins with >100 observations per 1° grid bin for 1950–2007. Maximum is centred on KI. Dark lines are SST isotherms 10–26°C (data from HadISST, n.d., Rayner *et al.*, 2003). White pixels lack enough observations. Each pixel is positioned so that the latitude-longitude grid bin that it represents is on its SW corner

location and show smaller SST patches colder than 9°C extending along the island chain from approximately 45°N, 150°E to 48°N, 155°E, which includes the fog maximum observed by the ship.

Grid bin values greater than 55% are oriented along a line extending from southwest to northeast, which closely follows the shallow shelf along the central portion of the Kuril Island chain (Figure 5). Of the 11 grid bins greater than 50%, only one (47°N, 151°W) is not centred over the shelf, and it is partially over the shelf. With one exception, all grid bins not over the shelf have occurrences less than 50%. Thus, shallow water is a significant factor for the increased fog occurrence, which Tokinaga and Xie (2009) attribute to tides mixing colder water with surface water.

The large-scale fog occurrence distribution is related to ocean surface currents. The area with grid bin fog values greater than 30% (one-half of the centred maximum grid bin value) extends eastward from the maximum across a majority of the Pacific to beyond 160°W. The boundaries of this feature are within the North Pacific sub-polar gyre (Tomczak and Godfrey, 2003) and are related to the SST field (the isotherms are shown in Figure 3). The southwest side of the gyre heads due east, which coincides with the southern edge of the fog occurrence maximum. This area is

FIGURE 4 Grid bin values central to the Kuril Island JJA fog maximum as percent of ICOADS fog observations at grid bins with >100 observations per 1° grid bin for 1950–2007. Shaded bins have values greater than 0.67 times the highest grid bin value. Greatest grid bin value is 60% at 47°N, 162°E

N	148 E		150 E		152 E		154 E		156 E		158 E		160 E		162 E	
52	39	36	35	31	26	31	35	34	25	22	31	19	21	27	27	30
	36	34	42	40	37	30	35	42	30	27	28	25	28	30	34	33
50	35	33	32	39	39	42	40	41	39	34	32	34	31	33	37	36
	32	29	35	42	43	43	43	48	44	41	38	41	44	43	40	39
48	30	34	36	40	47	46	58	56	51	43	41	49	46	44	42	36
	30	27	38	43	53	60	59	51	48	48	46	47	44	43	41	37
46	19	19	31	51	60	54	49	48	49	45	45	43	43	37	35	35
	30	34	43	54	47	45	47	48	42	42	39	39	36	34	35	33
44	39	49	44	44	41	43	44	40	31	33	33	32	31	30	32	32
	43	46	39	41	40	37	33	29	25	28	27	29	29	34	35	33
42	37	42	37	36	32	26	24	24	24	28	29	29	31	28	29	30
	32	33	30	23	20	19	18	21	23	24	25	26	26	24	25	24
	22	19	15	14	14	15	14	16	17	18	18	17	18	17	20	21

%
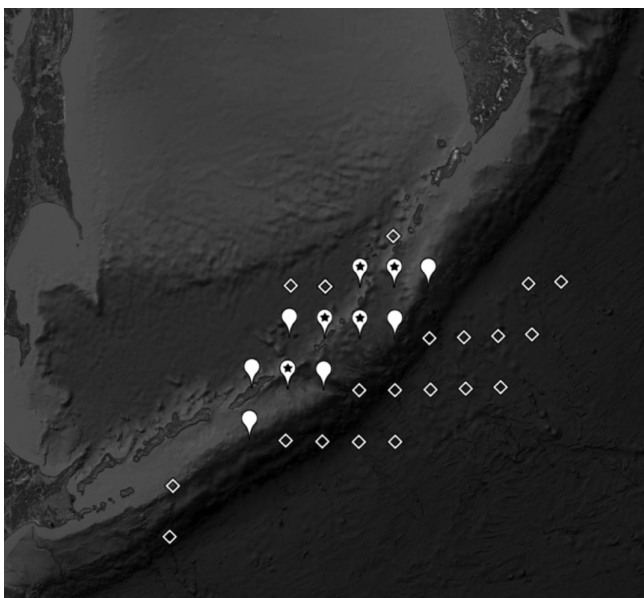|	
55–60	(darkest)
50–54	
45–49	
40–44	

FIGURE 5 Greater fog occurrences in the Kuril Island maximum on ocean bottom topography. Symbols representing fog values are on the centre of the grid bin location. Bulbs with a star are between 55 and <60%. Blank bulbs are between 50 and <55%. Diamonds are between 45 and <50%. Bottom topography can be found at https://www.google.com/earth/ (source Google Earth). Lightest depths around islands are less than 200 m. Darker depths of image are greater than 4,000 m

temperature inversion is important for fog occurrence in this area.

The lowest seasonal fog occurrence in the KI occurs in DJF, when values are less than 3% and there is no significant occurrence maximum. In other seasons, there is a maximum, with values between those in JJA and DJF (Table 3, Dorman *et al*., 2017).

While shallow water, SST and surface currents are coincident with the fog distribution, it is the seasonal surface wind field that determines whether it is warm, moist air over cool water that encourages fog or cold air over warmer water that suppresses it. The 1950–2007 North Pacific High JJA sea level pressure centre is centred at 36°N, 145°W (Dorman *et al*. (2017)), and the monsoon low pressure is centred over Eurasia (Ramage, 1971), causing surface air to flow northward over the warm Kuroshio current to absorb moisture, and then over a negative SST gradient in the Oyashio Current, and finally over the KI. In contrast, the DJF sea level pressure field changes to a low that is centred near 51°N, 172°E (Dorman *et al*. (2017)), and the monsoon high is centred over Eurasia (Ramage, 1971), causing cold, dry surface air to flow off land toward the south-southeast over the Okhotsk Sea and Oyashio Current, which inhibits fog formation over the KI.

5.3 | Okhotsk Sea

Summer is the peak fishing and resupply season in the Okhotsk Sea, which results in the greatest seasonal ship coverage. In contrast, DJF data are missing when northern portions of the Okhotsk Sea are missing ship observations due to sea ice and winter storms.

The occurrence of fog in the Okhotsk Sea is as great in JJA (Table 3) as it is for the KI, although the two are separated by a minimum fog zone over deep water that separates the Kuril Island chain from the Okhotsk Sea (Figure 3). Fog values in the Okhotsk Sea range from 25 to 55%, with the

bounded by a steep SST gradient, with higher temperatures to the south. As the sub-polar gyre currents turn north along the eastern side of the Pacific, the SST gradient and fog occurrence decrease toward the east.

A stable atmosphere capping fog in JJA is common within the maximum over KI. A long-term study on Hokkaido Island, which is on the southwest end of the Kuril Island chain, found that coastal fog always occurs with southerly winds and an air temperature inversion, and inversions do not occur without fog (Sugimoto *et al*., 2013). Haraoka *et al*. (1995) confirm that a low-level air

highest values occurring on the northwest side. The highest values are isolated maxima over local shallow regions, which were confirmed by Tokinaga and Xie (2009), who found that the maxima coincided with SST minima caused by tidally driven upwelling.

The season of lowest fog occurrence is DJF, when most ship observations are 1–4%, with the highest values scattered across the western portion of the Okhotsk Sea. Winds and stability are similar in the KI, as discussed earlier.

5.4 | Sea of Japan

The Sea of Japan has distinguishing meteorological and oceanic characteristics, including a limited sea ice distribution during winter (Dorman *et al.*, 2004; 2005). The greatest fog occurrence occurs in JJA (Table 3) and is concentrated along the Russian coast between 130° and 140°E (Figure 6b). The largest occurrence is 28%, which lies over the Russian shelf, but similar values are found at 2–3 grid bins across the coast, which extends over deeper water. Fog occurrence decreases sharply from the Russian coastal maximum to less than 2% along the central Honshu coast. In the Sea of Japan, SSTs are warmest in summer, with the highest values in the strait between Korea and Japan, and coldest along the Russian Coast (Dorman *et al.*, 2004; 2005), which promotes greatest fog occurrence in this sea along this coast.

DJF fog patterns change substantially, as the highest ship fog reports are 2% or less and irregularly distributed along the northern coast of the Sea of Japan. Over the southern half of the Sea of Japan, the lowest fog occurrences exist in SON and DJF, when the values are less than 1%.

The surface wind pattern, stability and advection are similar to those in the KI discussed previously. Dashko and Yudin (1998) and Dashko and Varlamov (2003) reported that the Japan and Okhotsk Seas had related conditions causing fog: a summer monsoon, anti-cyclonic atmospheric circulation and cold SST zones. A significant difference between the two seas is that the Sea of Japan has a minimum SST and fog over both the shelf and neighbouring deep waters, while the Okhotsk Sea has elevated fog values only over the shelf and the greatest fog occurrences were over isolated depth minima, coinciding with SST minima caused by tidal mixing.

5.5 | Yellow Sea

Coastal China is distinguished by an unusually deep marine fog, often reaching a 1 km depth (Zhang *et al.*, 2009) and extending unusually far offshore compared to other marginal seas (Dorman *et al.*, 2017). The greatest grid bin fog value (18.3%) and median (9.1%) in the Yellow Sea occur in MAM and are followed closely by those in JJA, while the lowest median value occurs in SON (0.5%), followed by DJF (Table 3). A questionable JJA grid bin value of 22.8% occurs at 36°N, 120°E, which is more than twice the nearby grid bin values and is not representative of other Yellow Sea values. The MAM fog distribution extends farthest offshore, and greater occurrences are more concentrated near 33°N (Figure 6a). Grid bin values greater than ~0.5 times the maximum grid bin value lie over the shelf. Both MAM and JJA have lower and missing grid bin values along the north shore. In all seasons, the distribution of peak values is somewhat erratic.

Although DJF is a low fog season, weak values increasing above the background values extend along the entire Chinese coast (Dorman *et al.* (2017)). An isolated maximum lies over the southern region of the South China Sea over the shelf during DJF (5.6%) and is treated as a distinct maximum (Table 3).

In a review of the fog climate in the Yellow Sea, Zhang *et al.* (2009) characterized fog as primarily advective, with prevailing warm, moist winds from the south-southeast. Tidal mixing over the shelf lowers the SST and forms SST fronts that affect fog dynamics. Land-sea contrast and other factors frequently support a shallow atmospheric anticyclone over the Yellow Sea, with an air temperature inversion that caps the marine boundary layer, which is an important factor for fog at other locations. In a climatological study of fog along the west coast of Korea, Kim and Yum (2010) found that most sea fog occurred in JJA, followed by MAM, while
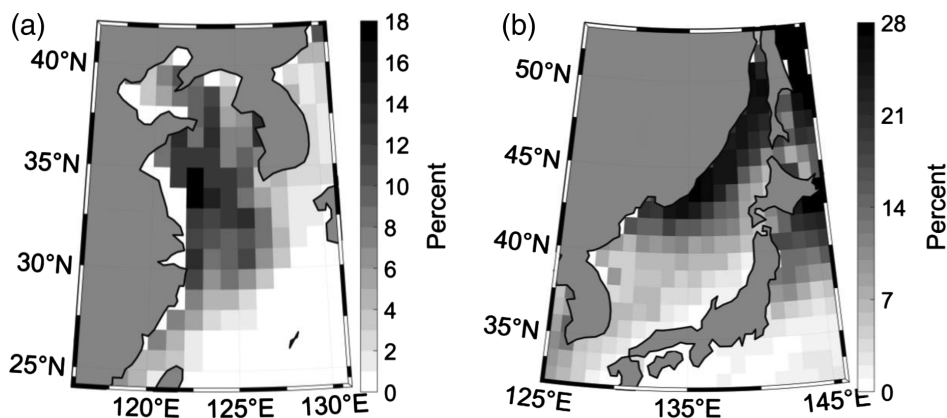

FIGURE 6 Yellow Sea MAM (a) and Japan Sea JJA (b) ICOADS percent of fog observations at grid bins with >100 observations per 1° grid bin for 1950–2007. White indicates insufficient data. Note different scales

a majority of fog occurred under air temperature inversion and high atmospheric pressure conditions, which is consistent with Zhang *et al*. (2009).

6 | NORTHWEST ATLANTIC OCEAN

6.1 | Introduction

Fog maxima in the GB and the nearby fog maximum along Nova Scotia, which are separated by a fog minimum (Table 4), are central ideas in this section. Both share some distinct oceanographic and meteorological conditions (Townsend *et al*., 2006). A comparison of ship fog with other observations in this area is presented in Section 3.

6.2 | Grand Banks

The second greatest marine fog occurrence maximum lies in the northwest Atlantic over GB during JJA, with the highest grid bin value of 45% at 44°N, 49°W (Figure 7 and Table 4). The structure of the maximum is systematic, with the highest values in the centre and smaller values extending further away (Figure 8). Decreasing values extend both westward along southern Newfoundland and toward the northwest into the Labrador Sea. Unlike the KI maximum, the GB maximum does not extend far across the Atlantic and only reaches approximately 40°W, 47°N.

In DJF, basic fog occurrence patterns in GB are similar to those in JJA, but all values are much smaller, as this is the seasonal minimum (Figure 9). The maximum fog occurrence in this season remains centred over GB, with a peak value of 13.1% at 45°N, 49°W.

During JJA, the distribution of the highest grid bin values coincides with the shallow bathymetry of the GB (Figure 10). The centres of all nine grid bins with values greater than 40% (marked bulbs with stars in Figure 10) are

over the GB shelf (<200 m), as are all 17 of those with values of 35–40% (blank bulbs in Figure 10), with the exception of one at 45°N, 48°W, which has a portion of its area residing over the GB shelf. Of the 30 grid bins in the maxima centre with values of 30% to <35% (diamonds in Figure 8), only one is over a region with a deeper slope (45°N, 47°W), while two more are centred over a shallower slope (43°N, 49°W and 46°N, 45°W). Overall, the higher fog value pattern follows the GB shelf topography, with the greatest values residing next to the southeastern shelf edge.

As with the Northwest Pacific, there is a close relationship between JJA fog occurrence and SST. The large-scale, long-term average SST for JJA over the northwest Atlantic is represented by white isotherms in Figure 6. Note that the 22 and 16°C isotherms bend around the southern side of the maximum. The steepest SST gradient occurs at approximately 51°W and is just south of the maximum centre.

Satellite SST climatology (Mesias *et al*., 2007) shows that summer water over the GB has the highest values over the south and west sides and has a smooth gradient toward the lowest values on the northeast side. However, the most distinguishing feature is an SST gradient starting at the southern edge of the GB shelf and extending offshore, perpendicular to the shelf edge, with the strongest gradient in the inner 100 km and a more moderate gradient in the next 200–300 km. This SST gradient band follows the shelf edge around the GB. The intense SST gradient off the southern edge of the GB coincides with the greatest fog occurrence over the GB itself.

The North Atlantic sub-polar ocean gyre has an irregular shape (Tomczak and Godfrey, 2003), coinciding with a fog grid bin structure greater than 10%, but covers a smaller portion of the Atlantic compared to the Pacific. The portion of the gyre along the Labrador and Newfoundland coasts

TABLE 4 NW Atlantic Ocean fog occurrence maxima characteristics

		Highest occurrence		Mean 5 highest
Area	Season	(%)	(°Lat–Lon)	(%)
GB	JJA	45.0	44°N 49°W	43.4
	SON	17.7	45°N 49°W	15.5
	DJF	13.1	45°N 49°W	11.5
	MAM	26.4	43°N 50°W	25.2
Nova Scotia	JJA	47.1	43°N 66°W	41.1
	SON	14.3	45°N 67°W	11.7
	DJF	5.5	45°N 62°W	5.2
	MAM	21.3	44°N 60°W	20.0

N	56 W	54 W	52 W	50 W	48 W	46 W	44 W	42 W								
	19	25	28	31	18	15	9	14	15	12	15	14	12	14	12	11
54	13	19	21	24	30	27	17	15	13	11	10	11	11	12	13	14
	3	15	19	29	29	28	16	15	12	13	12	13	13	12	13	14
52	24	17	17	17	20	26	29	26	18	17	19	15	17	14	15	15
	15	15	16	15	19	23	29	34	32	26	22	21	15	13	10	9
50		8	11	19	20	35	34	35	31	24	20	16	15	12	12	
	Labrador		8	15	26	38	37	34	28	26	25	25	23	16	12	
48			15	15	24	28	33	34	36	38	34	34	31	20	13	
	24	27	26	27	32	31	33	33	40	42	43	37	37	34	23	18
46	28	29	30	33	35	37	34	36	39	42	44	36	32	22	13	8
	29	29	31	31	35	32	36	40	43	37	31	24	18	12	8	6
44	27	25	23	26	30	34	37	41	45	28	21	16	13	9	6	5
	18	18	17	16	18	26	30	33	31	23	13	7	4	3	3	3
42	8	7	8	6	7	10	13	17	17	13	7	3	2	2	2	2
	2	2	2	2	2	3	3	4	6	6	4	2	2	1	2	2

%	
■	40–45
▨	35–39
▦	30–34
▫	25–29
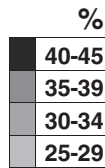
FIGURE 8 Grid bin values central to the GB fog maximum in JJA as a percent of ICOADS fog occurrence at grid bins with >100 observations per 1° grid bin for 1950–2007. Shaded values are 0.56 or greater of the maximum grid bin value. The greatest grid bin value is 45% at 44°N, 49°W. A grid bin with a mix of land and enough open water for ship operations has a value posted if >100 observations
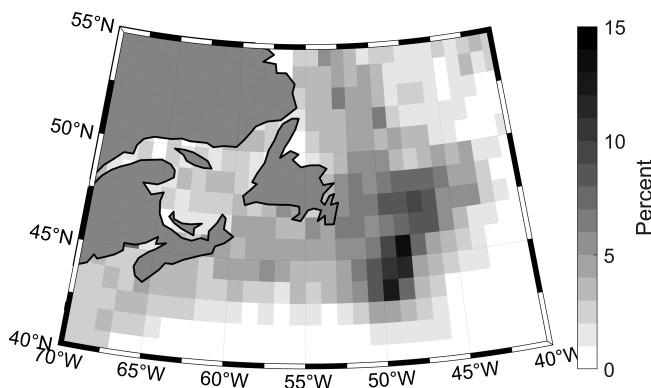

FIGURE 9 NW Atlantic DJF ICOADS percent of fog observations at grid bins with >100 per 1° grid bin for 1950–2007. GB and Nova Scotia maxima are included. White pixels have insufficient observations

contains a wide band of fog occurrence structures extending into the Labrador Sea.

The Labrador Current transports sub-polar water southward along Labrador, Newfoundland, and then over the GB (Chapman and Beardsley, 1989; Han *et al.*, 2008; 2011). Tidal currents are much stronger over the GB than the surrounding deep water and are greatest along the southeast portion of the GB (Han *et al.*, 2011). The most distinguishing oceanographic surface feature over the GB is that the highest fog grid bin values coincide with large tidal currents and mixing, which might be related.

As with the Pacific, shallow water SST and surface currents set the boundaries of Atlantic fog. The seasonal surface wind field determines whether warm, moist air flows over cool water and favours fog formation or the opposite occurs to suppress it. The JJA sea level pressure from 1950 to 2007 is dominated by the North Atlantic High pressure centred at 33°N, 36°W (Dorman *et al.*,

FIGURE 10 Greater fog occurrences in the GB maximum on ocean bottom topography. Symbols representing fog values are plotted on grid bin location. Bulbs with a star are between 40 and 45%. Blank bulbs are between 35 and <40%. Diamonds are between 30 and <35%. Bottom topography is from https://www.google.com/earth/ (source Google Earth). The bulk of the GB depths are less than 100 m. The sudden increase in depth at the edge of Brand Banks is 100–200 m. Darkest depths are greater than 2,000 m

2017), which causes the surface air to generally flow toward the north-northeast first (over the Gulf Stream, picking up heat and moisture) and then over a negative

SST gradient region in the cold Labrador Current. This role of warm air advection over colder sea water was discovered during early iceberg patrol ship observations over the GB (Taylor, 1917).

An air temperature inversion base mostly near 200–300 m, which leads to capping of GB fog, was measured by kite soundings from early iceberg patrol ships (Taylor, 1917). This area is capped by a mean stable lower atmosphere under the northwest portion of the North Atlantic anticyclone during JJA (Dorman *et al.* (2017)). One of the authors has followed JJA observations at Sable Island in the GB and Nova Scotia areas and found that fog occurred in two settings: in the deeply saturated centre of a travelling storm, with low cloud ceilings and precipitation, and the other around sunrise under the surface inversion and clear sky of a travelling anticyclone. Both could occur within a few days of each other.

6.3 | Nova Scotia

The eastern U.S. and Canadian coasts are divided by land projections separating distinctive meteorological and oceanographic areas (Townsend *et al.*, 2006) with unique fog patterns (Dorman *et al.* (2017)). During JJA, fog occurrence is less than 1% from Florida to Cape Hatters, North Carolina, and the majority is 1–5% from Cape Hatteras to Cape Cod, Massachusetts (Dorman *et al.* (2017)). In contrast, there is much greater fog occurrence northeast of Cape Cod, which is largely over shelf water. This includes a maximum fog grid bin value of 47% off the coast of southwest Nova Scotia during JJA (Figures 7 and 11). The maximum coincides with a small, tidally driven SST minimum (Garret and Loucks, 1976; Mesias *et al.*, 2007). The Nova Scotia fog maximum is separated from the GB maximum by minimum grid bin values less than 30% and coincides with deeper shelf channels. The lowest seasonal fog values occur during DJF (Table 4). The seasonal wind direction (advection) and

atmospheric stability near Nova Scotia are similar to those over GB.

7 | WIND-DRIVEN COASTAL UPWELLING

7.1 | Introduction

Marine fog maxima are found in five wind-driven coastal upwelling zones. The wind causes a minimum SST structure along the coast that dominates the lower atmosphere and clouds. Four upwelling regions lie along the eastern sides of the North and South Pacific and the North and South Atlantic Oceans, where subtropical anticyclones centred over water are adjacent to land (Boucher, 1975; van Loon, 1984). Equatorward surface winds along the coastline on the east side of the anticyclone push surface water offshore, which causes colder, deeper water to upwell to the surface over the continental shelf. The coldest SST occurs over the inner shelf and within 1 km of the beach (Smith, 1968; Beardsley *et al.*, 1987; Tomczak and Godfrey, 2003). Atmospheric hydraulic effects accelerate the surface winds around capes to increase upwelling and further lower SST (Koračin *et al.*, 2004; Dorman *et al.*, 2013). Mid-level air flow around the eastern side of the anticyclone subsides, forming a warm, dry air temperature inversion and capping cold, moist marine air while the surface air temperature is controlled by the SST. The cold, upwelled water causes a greater temperature difference between the marine air and the base of the inversion, as opposed to if there was no upwelling. The air temperature inversion is documented along the California-Oregon (Dorman *et al.*, 2000), Peru (Stuart and Wirfel, 1980; Enfield, 1981), northwest Africa (von Ficker, 1936; Stuart and Wirfel, 1980), and southwest Africa (von Ficker, 1936; Jury, 1985) regions. A fifth upwelling zone is located along southeast Arabia during the summer monsoon, with winds toward the northeast (Schott and McCreary, 2001;
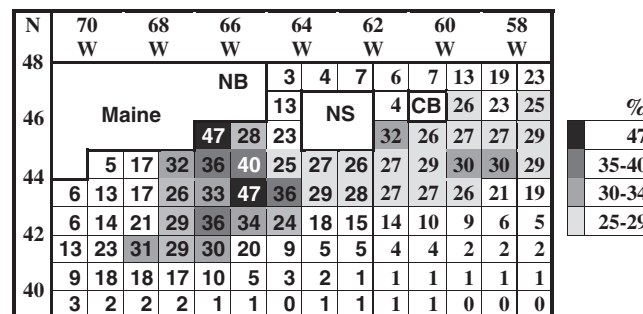
N	70 W	68 W	66 W	64 W	62 W	60 W	58 W							
48				NB		3	4	7	6	7	13	19	23
46	Maine						13	NS		4	CB	26	23	25
			47	28	23				32	26	27	27	29
44	5	17	32	36	40	25	27	26	27	29	30	30	29
	6	13	17	26	33	47	36	29	28	27	27	26	21	19
42	6	14	21	29	36	34	24	18	15	14	10	9	6	5
	13	23	31	29	30	20	9	5	5	4	4	2	2	2
40	9	18	18	17	10	5	3	2	1	1	1	1	1
	3	2	2	2	1	1	0	1	1	1	0	0	0

	%
(black)	47
(dark grey)	35-40
(grey)	30-34
(light grey)	25-29

FIGURE 11   Grid bin values central to the Nova Scotia fog maximum in JJA as percent of ICOADS fog observations at grid bins with >100 observations per 1° grid bin for 1950–2007. Shaded bins have values greater than 0.53 of the highest grid bin value. The highest grid bin value is 47.1% at 43°N, 66°W which is off the SW tip of Nova Scotia. A grid bin with a mix of land and enough open water for ship operations has a value posted if >100 observations. CB, Cape Breton Island; NB, New Brunswick; NS, Nova Scotia

TABLE 5 Wind-driven coastal upwelling zones fog occurrence maxima characteristics

Area	Season	Highest occurrence		Mean 5 highest (%)	N position (°Lat–Lon)	S position (°Lat–Lon)
		(%)	(°Lat–Lon)			
California-Oregon	JJA	16.6	38°N 123°W	14.4	44°N 124°W	37°N 122°W
	SON	14.5	42°N 124°W	12.6	44°N 124°W	36°N 121°W
	DJF	8.1	34°N 118°W	6.8	47°N 124°W	33°N 117°W
	MAM	7.4	42°N 124°W	5.5	44°N 124°W	34°N 118°W
Namibia-S. Africa	JJA	7.4n	24°S 14°E	5.8n	20°S 13°E	25°S 15°E
		10.0s	30°S 17°E	8.6s	26°S 15°E	31°S 17°E
	SON	18.3n	25°S 15°E	8.2n	23°S 14°E	26°S 15°E
		14.3s	29°S 17°E	10.4s	28°S 16°E	30°S 17°E
	DJF	19.2n	25°S 15°E	9.0n	25°S 14°E	28°S 15°E
		13.7s	29°S 17°E	12.0s	28°S 16°E	30°S 17°E
	MAM	24.8n	25°S 15°E	13.2n	23°S 14°E	27°S 15°E
		22.4s	30°S 17°E	16.2s	28°S 16°E	33°S 18°E
Peru	JJA	1.8	18°S 75°W	1.6	6°S 81°W	18°S 72°W
	SON	2.3	10°S 78°W	1.9	5°S 82°W	14°S 77°W
	DJF	7.9	14°S 76°W	4.6	12°S 77°W	15°S 75°W
	MAM	5.8	12°S 77°W	2.3	12°S 77°W	14°S 77°W
Morocco	JJA	4.7	29°N 11°W	3.2	31°N 10°W	28°N 12°W
	SON	3.1	30°N 10°W	2.6	32°N 9°W	28°N 12°W
	DJF	1.6	28°N 12°W	0.7	29°N 11°W	28°N 12°W
	MAM	2.1	32°N 9°W	1.2	32°N 9°W	29°N 11°W
Arabia	JJA	3.5	19°N 57°E	1.9	19°N 57°E	22°N 59°E

Note: Positions are the limits along the coast containing fog grid bin value with approximately one half the highest value of that centre or greater. The Namibia-South Africa maximum consists of two centres labelled n and s. No statistics are given for Arabia for SON, DJF and MAM because there is no significant fog maximum during these seasons.

Tomczak and Godfrey, 2003). Here, surface divergence causes subsiding air and an air temperature inversion (Ramage, 1971; Dwivedi *et al.*, 2016). For all five zones, there is a minimum SST over the inner shelf and an air temperature inversion capping a marine layer containing any fog.

Fog occurrence statistics along the coast extents for the 5 upwelling fog maxima are shown in Table 5, and the distributions are shown in Figure 12. In all cases, fog is greatest along the coast and decreases to less than one half of the coastal grid bin value within 2–3 grid bins from the coast. As the coldest water exists along the coast, grid bins with the greatest occurrences can be obscured by the land mask in the figures. Therefore, tables of individual pixel values are presented for two sites to more clearly show the distribution along and across the coast.

7.2 | California-Oregon

A fog maximum with a strong coastal upwelling zone is found along the northern California-southern Oregon coast during JJA (Table 5). This maximum extends along the coast

from 37 to 44°N, with grid bin values greater than half of the highest grid bin value and one or two grid bins across the coast (Figure 12a). The structure of this feature is more easily seen with the values in Figure 13. The maximum grid bin value is 16.6% at 38°N and decreases southward, which causes the fog to be significantly less along the central California coast (35°–36°N) and near the background values south of 34°N.

During DJF and MAM, upwelling is absent or reduced, and the atmosphere shifts to less stable synoptic patterns with frontal passages (Beardsley *et al.*, 1987; Dorman *et al.*, 1995), causing the lowest frequency of fog seasons (Dorman *et al.*, 2017). In DJF, fog occurrence is more uniform over the ocean rather than concentrated along the coast, which it is during the summer. The values herein are consistent with a coarser, ship-based fog study near California (Filonczuk *et al.*, 1995).

The JJA SST from 1950 to 2007 is shown in Figure 14a. A narrow SST minimum extends along the coast from 37 to 43°N, which is generated by wind-driven ocean upwelling, where mean surface wind speeds are
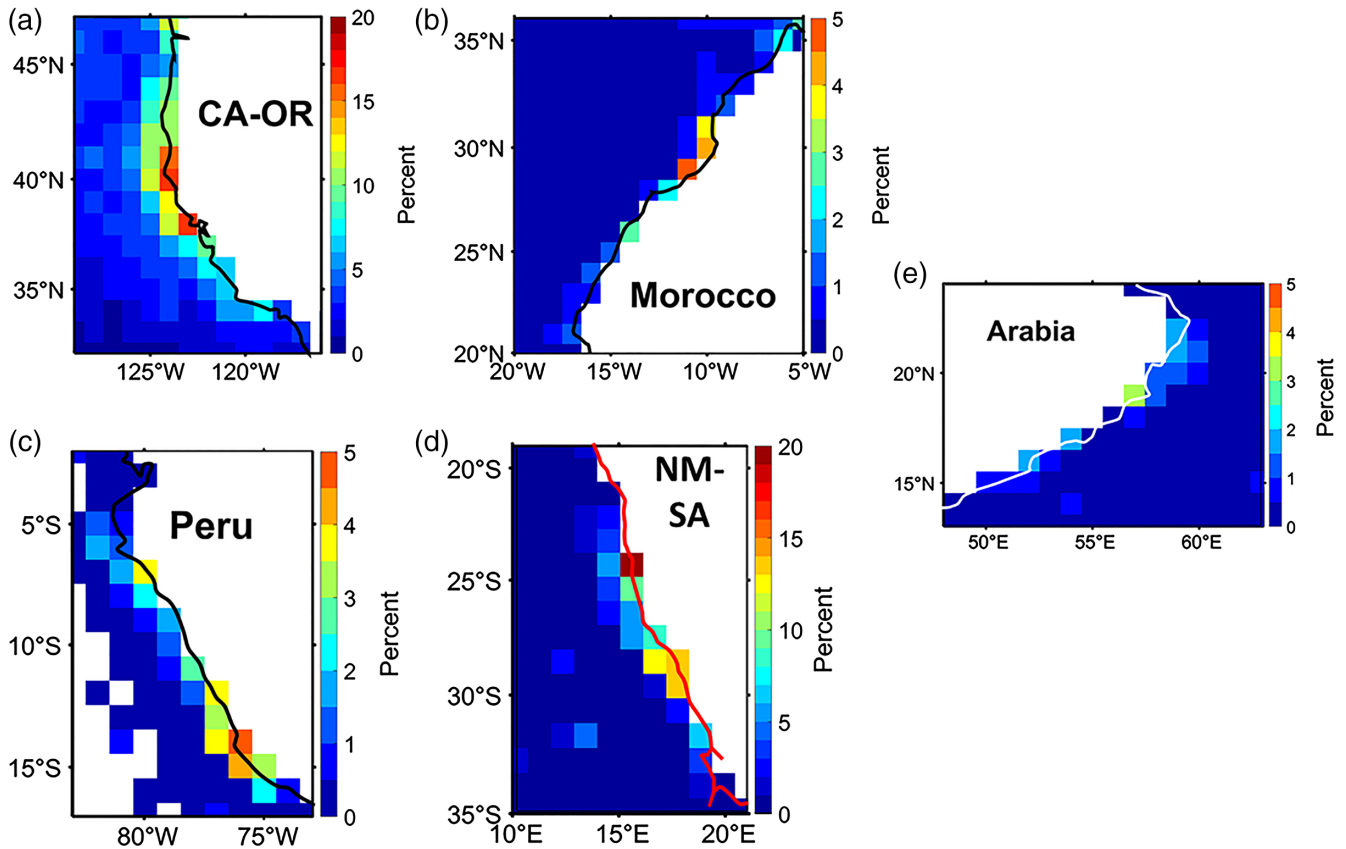
FIGURE 12   Wind-driven coastal fog seasonal ICOADS percent of fog observations at grid bins with >100 observations per 1° grid bin for 1950–2007. Season for California-Oregon, NW Africa and Arabia is JJA while it is DJF for Peru and Namibia-Southwest Africa. A grid bin with a mix of land and enough open water for ship operations has a value posted if >100 observations. White pixels do not have enough observations. Note colour bar scale differences [Colour figure can be viewed at wileyonlinelibrary.com]
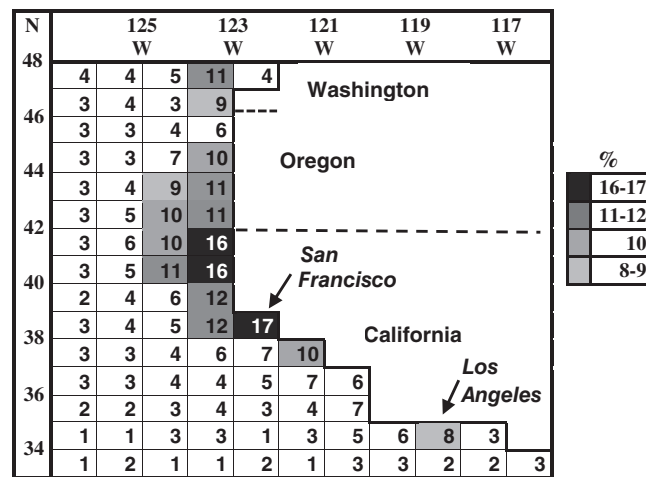
FIGURE 13   Grid bin values central to the California-Oregon fog maximum in JJA as percent of ICOADS fog observations at grid bins with >100 observations per 1° grid bin for 1950–2007. Shaded bins have values greater than 0.48 of the highest grid bin value. The fog maximum consists of grid bins that are contiguous and with values greater than 8.5%. The highest grid bin value is 16.6% at 38°N, 123°W. A grid bin with a mix of land and enough open water for ship operations has a value posted if >100 observations

greatest (Koračin *et al.*, 2004; Dorman *et al.*, 2013). The 16°C SST minimum almost completely underlies the grid bins with fog values greater than half the greatest grid bin value for the fog centre. Weaker mean winds in JJA extend a warmer SST minimum southward along the central California coast to near 34°N. Cross coast winds along the
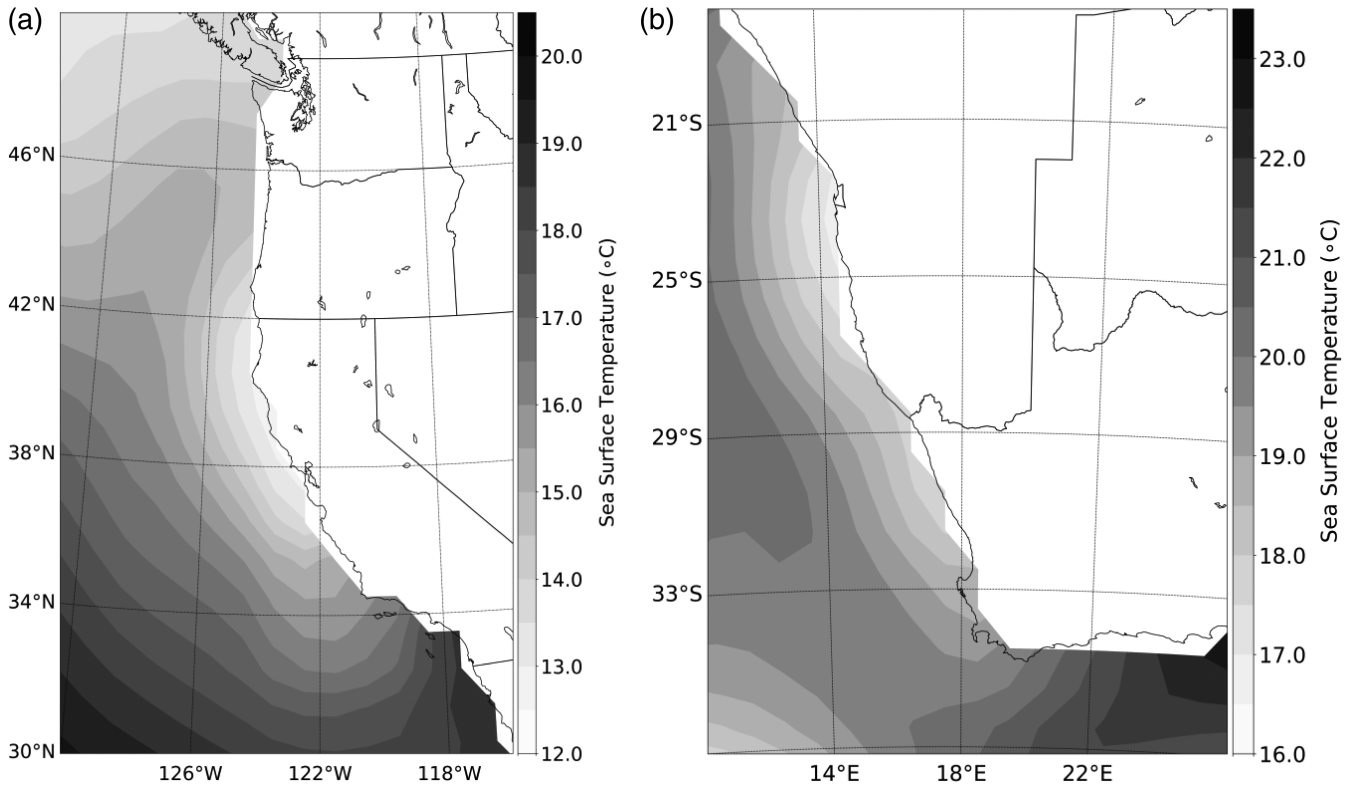
FIGURE 14 California-Oregon JJA (a) and Namibia-South Africa DJF (b) sea surface temperature from 1950 to 2007. Units are °C. Data source is HadISST (Rayner *et al.*, 2003)

Southern California Bight between 33° and 34°N do not support strong upwelling or a minimum temperature along the coast (Dorman and Koračin, 2008). The California-

Oregon coastal SST minimum is weakened in SON and MAM and eliminated in DJF. Thus, the SST is strongly linked to fog occurrence along the California-Oregon coast.
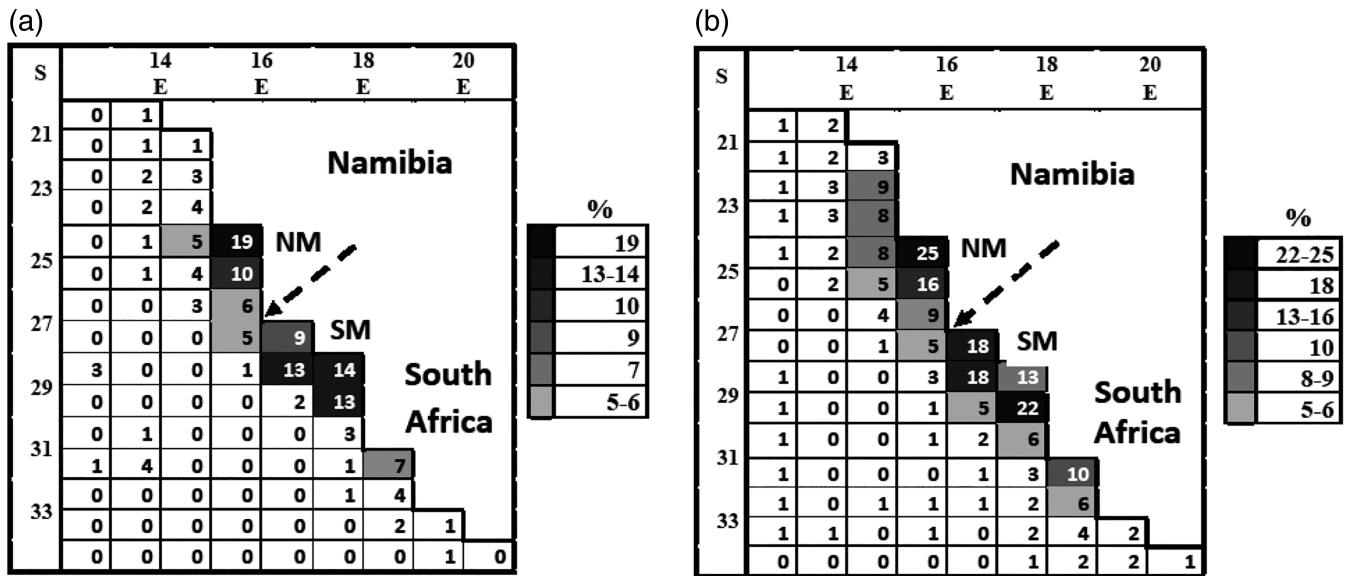
FIGURE 15 Grid bin values central to the Namibia-South Africa fog maxima as percent of ICOADS at grid bins with >100 observations per 1° grid bin for 1950–2007. In DJF (a), the northern maximum (NM) includes values greater than 0.5 times the second highest value (9.5%) of this centre. The highest grid bin value is 19.2% at 25°S, 15°E. The southern maximum (SM) includes values greater than 0.49 times the highest grid bin value of this maximum (13.7% at 29°S, 17°E). In MAM (b) the highest grid bin value in the NM is 24.8% (25°S, 15°E) and the highest grid bin value in SM is 22.4% (30°S, 17°E). Shaded values are greater than 0.20 of the highest grid bin value in that maximum. Dashed line marks the subjective boundary between the two maxima

7.3 | Namibia-South Africa

Coastal Namibia-South Africa is unusual compared to other wind-driven coastal upwelling fog regimes, as upwelling lasts year-round with two SST minima (DJF in Figure 14b). Each season has two fog occurrence maxima (Table 5), one located over each SST minima (Dorman *et al.* (2017)). The second highest grid bin seasonal value occurs in DJF (i.e. the climatological warm season), where the spatial distribution of fog has two peaks separated by a minimum (Figures 12d and 15a). Unlike the other coastal upwelling fog zones, the greatest fog values occur in MAM, with the highest values of 24.8% at 25°S, 15°E and 22.4% at 30°S, 17°E (Table 5 and Figure 15b). The JJA cold season has the least amount of fog, which occurs when the equatorial edge of the fog maximum is farthest north (20°S). In all seasons, the greatest ship grid bin fog value in each maxima region is up to a factor of 3 times greater than adjacent values; therefore, the values are provisional, as they are not confirmed by ship observations, which contrasts other upwelling fog regimes.

7.4 | Satellite measurements over wind-driven coastal upwelling zones

At present, satellite measurements are of low cloud and fog (SLC&F) together. The SLC&F distribution for June–September along the California-Oregon coast (Torregrosa *et al.*, 2016) has the greatest occurrence (>50%) and broadest cross coast section (>400 km) along 35°N. To the north, occurrences decrease to 33% and narrow to regions approximately 100 km along 41°N. In contrast, the ship fog maximum extends across only 1 or 2 grid bins offshore and is situated along the coast in the SLC&F moderate occurrence area, where the greatest ship grid bin value is 16.6%, while the SLC&F value is 46% (Table 1). Away from the ship maximum, the SLC&F occurrence values are ~10 times greater than the ship values. A rather similar SLC&F (Cermak, 2012) and ship fog distribution (Dorman *et al.* (2017)) occurs along the Namibia-South African coast. However, in this case, satellite observations were taken at the cloudiest time of day (7 LST), causing the fog occurrence to be reduced by an uncertain factor when compared with 24-hr ship observations (Gultepe *et al.*, 2007). This results in the satellite value being similar to the greatest value of the northern ship fog grid bin (Table 1). Offshore of the coastal ship maxima, SLC&F values are more than 100 times greater. Overall, ICOADS ship fog reports are consistent with SLC&F observations in that there are less of the former than the latter, although they are most similar over the ship coastal maxima. Away from the coast, SLC&F observations are dominantly stratus (Combs *et al.*, 2010), which is consistent with very low ship fog values away from the coast.

7.5 | Summary of fog occurrence in wind-driven upwelling regions

A relationship was found between fog occurrence and SST in five wind-driven coastal upwelling areas. As noted previously, four areas lie along the eastern side of an oceanic subtropical high, and the fifth exists under the summer monsoon. All areas have a cool, moist, surface atmospheric marine layer capped by an air temperature inversion with a low altitude base. There is one upwelling SST coastal minimum with a fog maximum centred over it for all regions, excluding the Namibia-South Africa region, which has two SST and two coinciding fog maxima in all seasons. The maximum seasonal fog occurrence for the four upwelling areas exists during the warm season (JJA or DJF), whereas for Namibia-South Africa, it exists during MAM. To present areas under comparable conditions, the warm season maximum grid bin fog and minimum SST are shown in Figure 16 with the best fit line. The SST minimum shows a closed isotherm with the lowest value based on an SST analysis with a 1°C contour interval (HadISST, n.d.; Dorman *et al.*, 2017). A modification is observed for Namibia-South Africa, which has two maxima. The result is that a lower upwelling SST is linked to greater fog occurrence. The hypothesis is that stronger coastal winds cause a lower SST, lower marine layer air temperature, lower air temperature base height and greater strength of the capped air temperature inversion, which are more conducive to the formation and persistence of fog.
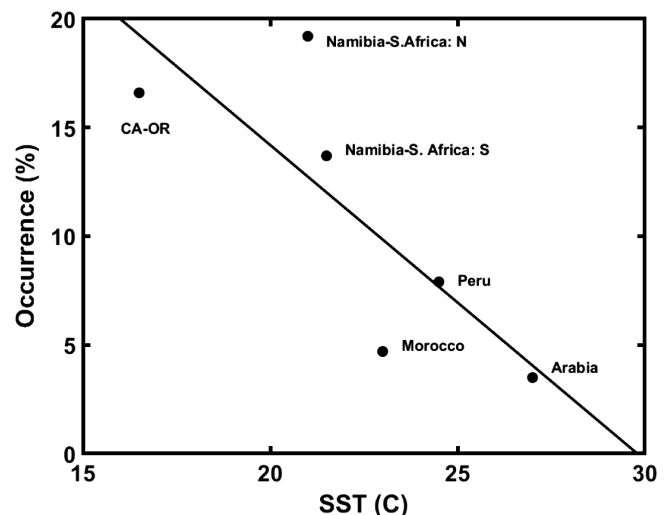

FIGURE 16 Wind-driven upwelling warm season fog occurrence maximum highest grid bin value versus SST minimum isotherm based on an analysis of SST (HadISST, n.d.; Dorman *et al.*, 2017). The line is a best fit of the data. Namibia-South Africa has two upwelling centres with a fog maximum over each

TABLE 6 NE and SW Atlantic fog occurrence characteristics

Area	Season	Highest occurrence		Mean 5 highest (%)	Median area (%)
		(%)	**(°Lat–Lon)**		
North Sea	JJA	5.8	59°N 2°W	5.5	3.1
	SON	4.1	59°N 1°W	3.9	2.0
	DJF	7.3	51°N 3°E	5.8	2.4
	MAM	9.7	55°N 5°E	8.3	4.6
Baltic Sea	JJA	(16.4) 11.6	(64°N 23°E) 4°N 24°E	(11.0) 8.9	1.8
	SON	7.7	65°N 22°E	6.5	2.1
	DJF	12.5	61°N 17°E	10.4	3.9
	MAM	17.2	61°N 17°E	14.8	5.4
Argentina	JJA[a]	11.1	42°S 57°W	10.3	—
	SON[a]	(17.2) 13.3	(41°S 58°W) 41°S 56°W	(13.0) 11.7	—
	DJF	9.8	43°S 59°W	8.5	—
	MAM[a]	10.9	41°S 56°W	10.2	—
Scotia Sea	JJA	—	—	—	—
	SON	—	—	—	—
	DJF[a]	28.2	60°S 54°W	23.8	—
	MAM	—	—	—	—

Note: The North Sea median calculation is over 52°N–59°N, 2°W-8°E. Five highest grid bin values include this median area and grid bins north and east of 50°N 1°E. The Baltic Sea area for both the median and five highest grid bin values is 54°–65°N, 10°–29°E, while excluding 64°–66°N, 10°–13°E. parentheses enclose both an apparently excessive value compared to neighbouring grid bins and the mean of the five highest that includes this value. The second value in the Baltic Sea mean 5 highest is the mean of the second to sixth highest values.

[a]Some grid bins in maximum missing data.

8 | NORTHEAST AND SOUTHWEST ATLANTIC OCEAN

8.1 | Introduction

This section presents fog maxima for the North Sea, Baltic Sea, Argentina, and Scotia Sea (Table 6). Eastward propagating cyclones and anticyclones are the dominant weather patterns of these regions.

8.2 | North Sea and Baltic Sea

European coastal waters include the North Sea and Baltic Sea. The Shetland Islands and Orkney Islands separate the North Sea from the Atlantic, while Denmark separates the North Sea from the Baltic Sea. Fog occurrences over these two seas have a modest seasonal signal, with the greatest frequency occurring in MAM (Table 6). The fog distribution over both seas in all seasons is somewhat irregular. In MAM, the highest values are in the south-central North Sea and along the northern coast of the Baltic Sea (Figure 17a). In SON (Figure 17b), the greatest amount of fog in the North Sea is found in the northwest region. In the Baltic Sea, the greatest values exist along the northern coast in all seasons (Table 6).

Both seas lie over the shallow continental shelf. For the North Sea, there is a weak relationship with depth (European Marine Observation and Data Network, 2016; National Centers for Environmental Information NOAA, n.d.), causing the greatest amount of fog to occur over broadly shallower waters in the south-central portion, but there is no clear relationship with SST. In the Baltic Sea, the coldest water and greatest fog occurrences are in the northern region (National Centers for Environmental Information NOAA, n.d.), which is characterized by irregular distributions of deeper water surrounded by shallower water (Seifert *et al*., 2001).

Findlater *et al*. (1989) and Lewis *et al*. (2004) reviewed North Sea fog formation mechanisms, which include warm and cold advection. Baltic Sea fog events are also typically advective (Bendix, 2002). Both seas are dominated by travelling cyclones and anticyclones throughout the year (Boucher, 1975), which are likely responsible for the fog occurrence distribution.

8.3 | Argentina

A smaller and weaker version of the northern ocean fog maxima (KI and GB) extends along Argentina's shelf break and occurs under somewhat similar circumstances.
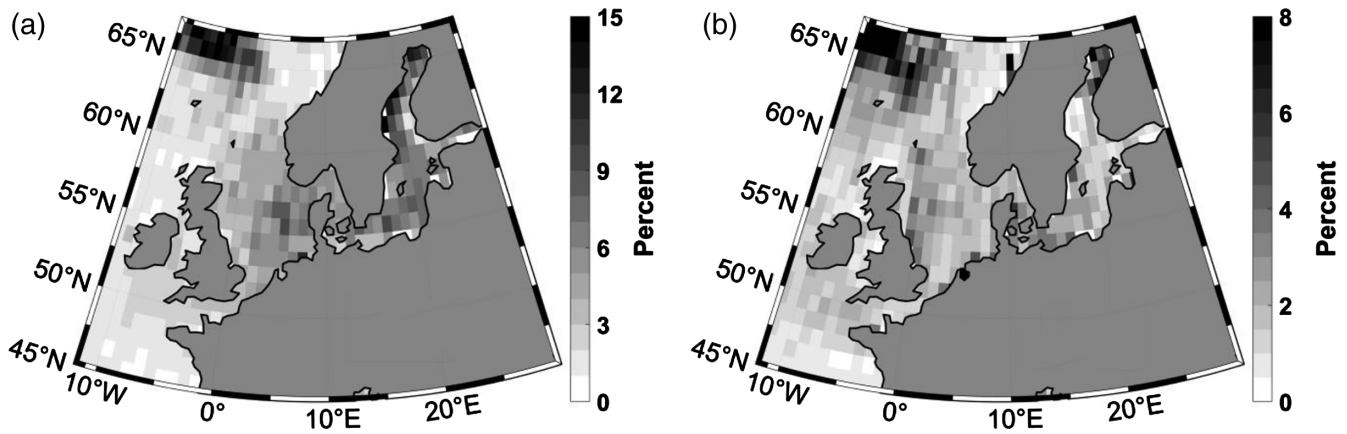
FIGURE 17 North Sea and Baltic Sea MAM (a) and SON (b) ICOADS percent of fog observations at grid bins with >100 observations per 1° grid bin for 1950–2007

However, ship data coverage is low and sporadic, resulting in erratic values. This maximum has an annual weak, marginal signal, with the highest values in SON and lowest in DJF (Table 6). Occurrences are especially erratic in SON, with a maximum grid bin value that is suspiciously high. The DJF distribution is shown in Figure 18, as it has the greatest number of observations and facilitates comparison with the warm season in the KI and GB. The fog maximum in Argentina extends from 45°S, 60°W to 38°S, 55°W (Table 6 and Figure 18). This is a linear feature, with the five greatest grid bin values along the continental shelf break (Dorman *et al.*, 2017), that lies over the cool equatorward Malvinas Current that follows the Argentinian continental shelf (Tomczak and Godfrey, 2003).

The SST gradient along the western side of the South Atlantic (1.2°C/100 km) is approximately one half that in the northern Atlantic (2.7°C/100 km; Dorman *et al.* (2017)). Off the coast of central Argentina, SST isotherms are oriented east–west but with a cold extension toward the northeast, creating a zonal minimum over the shelf break from 45°S, 59°W to 38°S, 55°W, which coincides with the fog maximum (Dorman *et al.* (2017); National Centers for Environmental Information NOAA, n.d.). The SST zonal minimum is due to wind-driven oceanic shelf-break upwelling (Valla and Piola, 2015; Carranza *et al.*, 2017), which is modulated by atmospheric storm winds associated with frontal passages.

The DJF mean sea level pressure gradient creates winds from west to northwest over this fog maximum, which causes the seasonally mean neutral advection or weak advection of warmer air over colder water (Dorman *et al.* (2017)). Unlike northern oceans, the South Atlantic subtropical high is too distant to have a direct effect on the seasonal wind direction; therefore, wind variations and stability are controlled by eastbound cyclones (Taljaard, 1972; Karoly and Vincent, 1998).

8.4 | Scotia Sea

There is a unique deep water fog zone with provisional maxima over the Scotia Sea (Figure 18). This fog centre has its maximum grid bin value at 60°S, 52°W and extends eastward over the eastward bound Circumpolar Current. The mean of the 5 highest occurrences is 23.8% (Table 6). This is a tentative fog maximum because the low number of
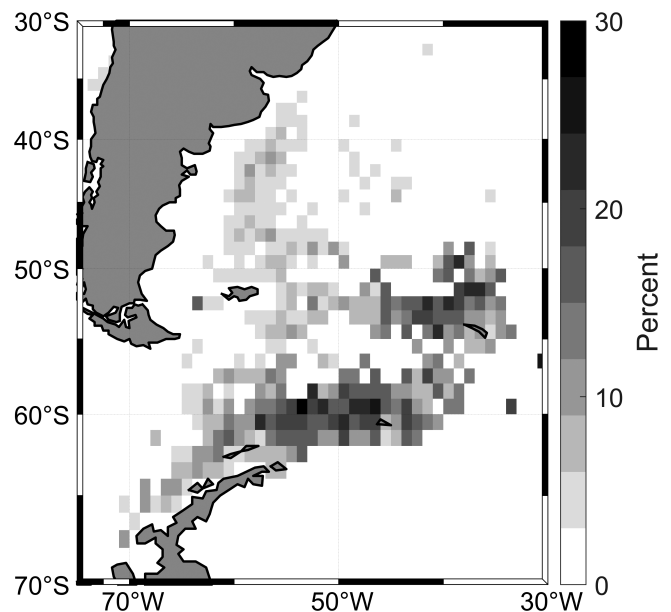

FIGURE 18 SW Atlantic-Southern Ocean DJF ICOADS percent of fog observations at grid bins with >100 observations per 1° grid bin for 1950–2007. A weak fog maximum is around 43°S, 59°W over the shelf along the Argentina coast. A stronger fog maximum is around 60°S, 54°W over the Scotia Sea/circumpolar current on the east side of the Drake Passage narrows between South America and Antarctica. In this season, fog greatest occurrence is at 60°S, 54°W. White pixels do not have sufficient observations

observations during this season and absence in other seasons prevents a more complete analysis.

Mean DJF SST isotherms over this area are oriented south-southwest to north-northeast (Dorman *et al.* (2017)). Strong eastbound winds are indicated by close, mean DJF sea-level pressure zonal isobars (Dorman *et al.* (2017)). It is likely that the progression of eastbound cyclones (Taljaard, 1972; Karoly and Vincent, 1998) controls fog occurrence in this area.

9 | TEMPORAL FOG CHANGES

In this section, the long-term variability and trends of sea fog are considered. The two greatest fog occurrence locations, the KI and GB, during JJA are presented, as they have the greatest number of observations and signal-to-noise ratios. For both locations, a contiguous rectangular area was chosen to overlay most of the domain centre. Each centre area was subdivided into 3° by 3° latitude–longitude areas, with JJA values from 1950 to 2007. Finally, a time series of 58 annual summer averages was created to examine temporal variability and trends. The fog maxima are compared with long-term climate indices to examine possible relationships. For the KI, Pacific Ocean variations are represented by the Pacific Decadal Oscillation (PDO; Newman *et al.*, 2016). First introduced by Mantua *et al.* (1997) as the leading empirical orthogonal function (EOF) of the North Pacific (20–70°N), SST monthly averaged anomalies are calculated as departures from the climatological annual cycle after removing global mean SSTs. The PDO represents the effects of different processes operating on different time scales that only partly represent direct atmospheric forcing by the North Pacific Ocean (Newman *et al.*, 2016). The amplitude of the PDO has a pronounced late summer–early fall minimum SST anomaly, with a centre that shifts toward the northwestern Pacific (Wang *et al.*, 2014). An annual JJA value was averaged from monthly PDO values (data source: JISAO PDO, n.d.; Mantua *et al.*, 1997). To better represent the variations, Pearson, Spearman, and Kendall correlations were

computed (Myers and Well, 2003; Gibbons and Chakraborti, 2010). The annual KI index has great interannual variability compared to the PDO, resulting in low correlations that are not significant (Figure 19 and Table 7). A 5-year moving average suppresses the interannual variation, improving the correlations to 0.55–0.79, which are significant according to the *p*-value.

The El Niño–Southern Oscillation (ENSO), which was reviewed by Guilyardi *et al.* (2009), is composed of irregular variations in SSTs and trade winds over the eastern tropical Pacific. El Niño occurs under weak trade winds and higher SSTs, while La Niña occurs under opposite conditions. Fluctuations in ocean temperatures during El Niño and La Niña are accompanied by even larger-scale fluctuations in air pressure between the western and eastern tropical Pacific, known as the Southern Oscillation. ENSO is teleconnected to the PDO, which is the result of a combination of different physical processes, including ENSO (Newman *et al.*, 2016). Here, we use the Niño 3.4 index calculated from Hadley SST data (Earth Systems Laboratory NOAA Niño 3.4, n.d.; Smith and Sardeshmukh, 2000) to characterize the ENSO signal. The annual 3-month averaged (JJA) ENSO index poorly follows larger scale changes in KI fog, with insignificant correlations (Figure 20 and Table 7). A 5-year moving average does not drastically change the correlation or significance.

Long-term GB variations are compared with the North Atlantic Oscillation (NAO), which was reviewed by Hurrell *et al.* (2013) and Stephenson *et al.* (2003). The NAO is the atmospheric sea level pressure difference between the Islandic Low and Azores High, a permanent feature that is weakest in JJA. This index is represented by monthly or seasonal pressure differences between a point in each of the pressure extremes. The index used here is created from the average JJA difference between the normalized sea level pressure over Gibraltar and the normalized sea level pressure over Reykjavik (Climatic Research Unit-Jones NAO Data, n.d.; Jones *et al.*, 1997). GB fog and NAO annual summer data track consistently with each other, with modest
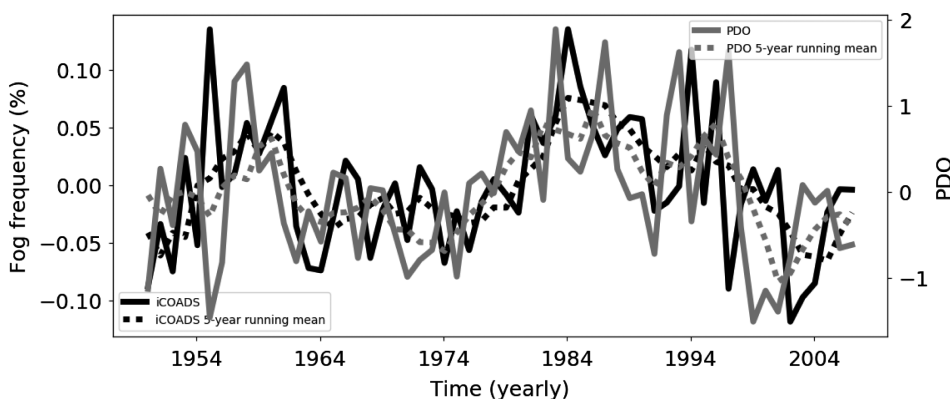

FIGURE 19 Annual JJA indices for Kuril Island centre fog occurrence (solid black curve) and the PDO (solid grey curve) for 1950–2007. A 5-year moving average of the Kuril Island fog centre is dashed black and PDO is dashed grey. See text for PDO data source

TABLE 7 Annual JJA correlations and *p*-values between fog centre detrended data and climate indices over 1950–2007 for three different correlation types (see text for explanation and references)
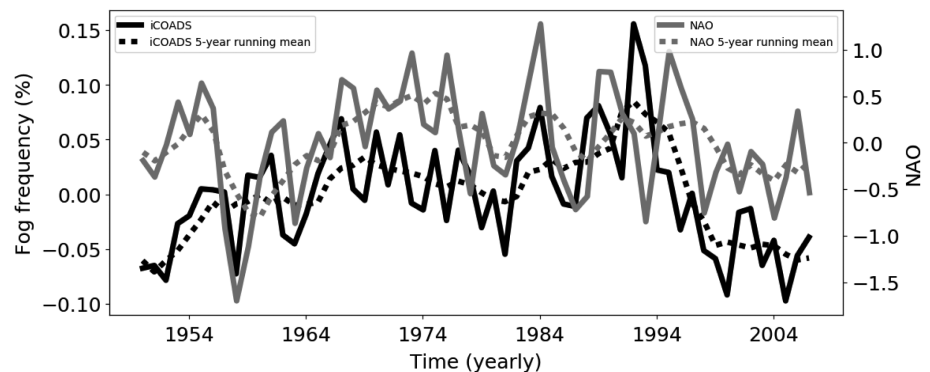
Fog centre	Climate index	Corr type	Corr	*p*	5 yr mov avg Cor	5 yr mov avg *p*
Kuril Is.	PDO	Pearson	0.139	0.298	0.786	2.54e−13
		Spearman	0.199	0.134	0.769	1.87e−13
		Kendall	0.135	0.134	0.549	1.17e−09
	ENSO3,4	Pearson	−0.147	0.268	0.070	0.601
		Spearman	−0.180	0.176	−0.000	0.975
		Kendall	−0.126	0.161	0.024	0.788
GB	NAO	Pearson	0.310	0.018	0.482	1.27e−04
		Spearman	0.352	6.77e−03	0.557	5.61e−06
		Kendall	0.244	6.87e−03	0.341	1.55e−04
	AMO	Pearson	−0.583	1.51e−06	−0.751	1.12e−11
		Spearman	−0.576	2.22e−06	−0.737	3.90e−11
		Kendall	−0.407	6.35e−06	−0.532	3.57e−09

FIGURE 20 Annual JJA indices for Kuril Island centre fog occurrence (solid black curve) and the ENSO (solid grey curve) for 1950–2007. A 5-year moving average of the Kuril Island fog centre is dashed black and ENSO is dashed grey. See text for ENSO data source
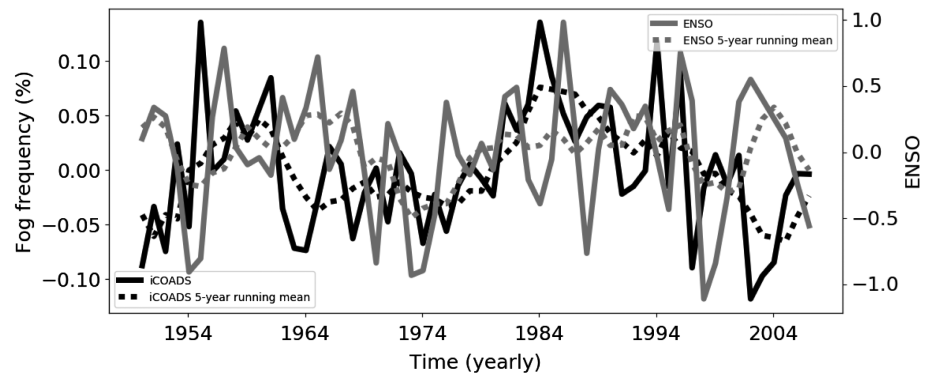
correlations ranging from 0.24 to 0.35 (Figure 21 and Table 7). A 5-year moving average improves the correlation to a range of 0.34–0.56, with lower P-values.

The Atlantic Multidecadal Oscillation (AMO; Hurrell and van Loon, 1997; Enfield *et al*., 2001; Knight *et al*., 2006; O'Reilly *et al*., 2017) has been identified as a coherent mode of natural variability occurring in the North Atlantic, with an estimated period of 60–80 years. It is based on the average SST anomalies in the North Atlantic basin (typically over 0–80°N). To remove the climate change signal from the AMO index, SST data are detrended at each grid bin, or the spatially averaged time series is detrended (Trenberth *et al*., 2017). To represent the AMO, the index used here is the Earth Systems Research Laboratory NOAA AMO (n.d.), which Enfield *et al*. (2001) unsmoothed and detrended from Kaplan SST V2 data (Kaplan, 2003). The ICOADS GB fog

FIGURE 21 Annual JJA indices for GB centre fog occurrence (solid black curve) and the NAO (solid grey curve) for 1950–2007. A 5-year moving average of the GB fog centre is dashed black and NAO-point is dashed grey. See text for NAO–point data source
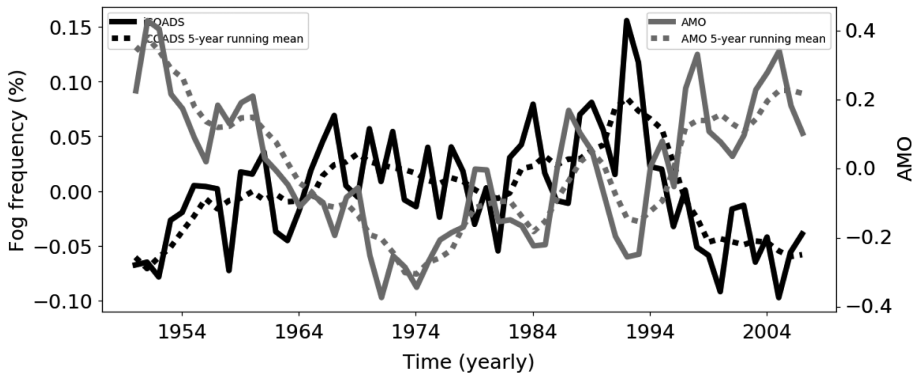
occurrence and AMO biannual summer data have an inverse correlation ranging from −0.41 to −0.58, with *p*-values less than 1.55e−06. A 5-year moving average improves the correlations to a range of −0.53 to −0.75, with *p*-values less than 3.90e−11 (Figure 22 and Table 7).

We now offer some plausible explanations for the results of the previous sections. The KI and GB fog maxima occur in similar climatic areas, which are between a large-scale semi-permanent atmospheric low and high (Hurrell *et al.*, 2013) and strong SST gradients between warm and cold currents in the Kuroshio/Oyashio and Gulf Stream/Labrador Current, respectively. During JJA, they are frequently in the path of storms moving toward the east-northeast (Climate Prediction Center, n.d.: Serreze *et al.*, 1997). As noted earlier in Section 9b, fog occurs in the centres of moving cyclones and anticyclones in this area.

The centre with the highest marine fog occurrence extending over the largest area lies over the KI, which is positively and strongly correlated with the 5-year moving average of the PDO index that was derived from the North Pacific SST over 20–70°N. The large-scale SST field in the North Pacific is known to be related to moving storms over this area. By extension, we assume that this includes moving anticyclones, and both are controlled by variations in the SST field and thus fog occurrence.

Focusing on the Atlantic, the NAO has modest, positive, 5-year moving averaged correlations with fog occurrence in the GB. North Atlantic storm tracks shift north during a positive NAO and south during a negative NAO (Serreze *et al.*, 1997). More northerly storm tracks cause proportionately greater flow from the south-southwest that is associated with warm, moist air flowing over colder water, which supports fog.

In contrast to the other fog centre with the same ocean indices, the AMO index is negatively correlated to the fog centre over the GB. The AMO is derived from Atlantic SSTs over 0–80°N. O'Reilly *et al.* (2017) report that drier and warmer air masses over northeast North America, including eastern Newfoundland, are associated with the warm

(positive) phases of the AMO (1931–1960, 1996–2010). Such air advected to Newfoundland and nearby GB has a larger dew point depression, which reduces fog formation. In any event, the magnitudes of the AMO correlations are significantly greater than those for the NAO, which suggests that the SST coverage of the North Atlantic is more important than the NAO two-point pressure field difference.

It is of note that the correlations of the PDO with the KI are of opposite sign but similar magnitude compared to the AMO correlations with the GB for the 5-year moving averages. In addition, the unsmoothed AMO correlations have average values and are significant, while the PDO correlations are low and insignificant. We surmise that the difference in sign is related to ocean differences, such as size and sub-polar gyres, although the physical pathway differences are uncertain. However, the size difference at the larger Pacific scale is apparent in the fog and sub-polar gyre of the KI, extending most of the way across the North Pacific (Figure 3), while the eastern extension of fog and sub-polar gyre in the GB is restricted to the western half of the Atlantic (Figure 7).

10 | SUMMARY AND CONCLUSIONS

Although fog occurrence over the non-polar oceans is only approximately 0.2%, there are significant distinct maxima on the west side of three ocean gyres (KI, GB, and Argentina) and secondary maxima on the western and eastern sides of northern oceans, as well as in coastal upwelling zones. The locations of fog frequency maxima correspond to shallow and cool SST waters, with tidal mixing, surface current gyres, the advection of moist and warm air over cool waters in summer, and a stable atmosphere capped by a low-level temperature inversion. Due to sharply decreasing differences in air and sea temperatures in winter, fog frequency is very low. Fog is usually a few hundred meters or so deep; however, it can reach more than a 1 km depth, such as over the South China Sea.

A summary of the two greatest fog frequency maxima (KI and GB) follows which one illustrates the main processes conducive to fog formation. For the KI, the highest maximum fog frequency is up to 60%. The centre maximum is located over the closed 10°C isotherm and some cold patches over shallow water caused by tidal mixing. Fog always occurs with southerly winds and a stable atmosphere capped by a low-level temperature inversion (Haraoka *et al.*, 1995; Sugimoto *et al.*, 2013). A synoptic setup with the North Pacific high and monsoonal low over Eurasia causes northward warm, moist airflow from the Kuroshio Current into the cold Oyashio current and over the KI. In contrast, during the synoptic setup in winter, the flow turns to an offshore direction, which prohibits fog formation.

For the GB, a major NW Atlantic maximum of fog occurrence of up to 45% exists over shallow waters less than 200 m deep. The summer North Atlantic high drives southerly flow, which becomes warm and moist over the Gulf Stream, and then creates negative SST gradients, including the cold Labrador Current. A low-level temperature inversion caps a stable planetary boundary layer and facilitates fog formation (Taylor, 1917).

An examination of possible climate trends in fog frequency for the areas with strongest signal-to-noise ratios (KI and GB) was conducted for this 58-year data series. Fog frequency at both of these two locations shows significant increasing trends. Since these trends could be related to short-term climate variability in the broader area, they were compared to the PDO and ENSO indices (KI) and the NAO and AMO indices (GB). The KI fog frequency is correlated with positive phases of the PDO but uncorrelated with ENSO. Both fog maxima are located between high and low sea level pressure centres. During positive phases of the PDO and NAO, pressure gradients increase, and in both cases, storm tracks move to the north, causing more warm and moist southerly flow and facilitating fog formation. However, the AMO is inversely proportional to fog frequency in the GB. A positive AMO phase is associated with dry and warm air over NE America, including the Newfoundland area, preventing fog formation.

Future studies are needed to further reveal relationships between fog frequency and short-term climate variability, differences between fog observations from ships versus coastal land stations, and relevant air-sea interaction processes at long-term scales. The recent development of fog detection algorithms using satellite data will shed more light on the worldwide characteristics of marine fog.

ORCID

Clive E. Dorman https://orcid.org/0000-0002-9866-3974
John Mejia https://orcid.org/0000-0001-6727-5541

REFERENCES

Bassem, E. (Ed.) (2015) *Metocean Climate Study Offshore Newfoundland & Labrador. Study Main Report.* Regional Trends and Comparisons with Other Regions, Vol. 2. C-CORE. Available at: http://exploration.nalcorenergy.com/wp-content/uploads/2016/09/Nalcor-Metocean-Study-Final-Report-Volume-1-04-06-2015.pdf [Accessed 01 May 2017].

Beardsley, R.C., Dorman, C.E., Friehe, C.A., Rosenfeld, L.K. and Winant, C.D. (1987) Local atmospheric forcing during the Coastal Ocean dynamics experiment. 1. A description of the marine boundary layer and atmospheric conditions over a northern California upwelling region. *Journal of Geophysical Research: Oceans*, 92 (C2), 1467–1488. https://doi.org/10.1029/JC092iC02p01467.

Bendix, J. (2002) A satellite-based climatology of fog and low-level stratus in Germany and adjacent areas. *Atmospheric Research*, 64, 3–18. https://doi.org/10.1016/S0169-8095(02)00075-3.

Boucher, K. (1975) *Global Climate*. New York, NY: Halsted Press ISBN: 0-470-09101-0.

Carranza, M.M., Gille, S.T., Piola, A.R., Charo, M. and Romero, S.I. (2017) Wind modulation of upwelling at the shelf-break front off Patagonia: observational evidence. *Journal of Geophysical Research: Oceans*, 122, 2401–2421. https://doi.org/10.1002/2016JC012059.

Cermak, J. (2012) Low clouds and fog along the South-Western African coast—satellite-based retrieval and spatial patterns. *Atmospheric Research*, 116, 15–21. https://doi.org/10.1016/j.atmosres.2011.02.012.

Chapman, D.C. and Beardsley, R.C. (1989) On the origin of shelf water in the middle Atlantic Bight. *Journal of Physical Oceanography*, 19, 384–391. https://doi.org/10.1175/1520-0485(1989)019<0384:OTOOSW>2.0.CO;2.

Climate Prediction Center (n.d.) *Storm Tracks.* Available at: http://www.cpc.ncep.noaa.gov/products/precip/CWlink/stormtracks/strack_NH.shtml [Accessed 01 June 2018].

Climatic Research Unit-Jones NAO Data (n.d.) *North Atlantic Oscillation (NSO).* Available at: https://crudata.uea.ac.uk/cru/data/nao/ [Accessed 01 June 2018].

Combs, C. L., Mazur, R., Clark, J., Norquist, M., & Molenar, D. (2010) An effort to improve marine stratus forecasts using satellite cloud climatologies for the Eureka, CA region. *Paper presented at 17th Conference on Satellite and Oceanography, Annapolis, MD.*

Available at: https://www.researchgate.net/profile/Debra_Molenar [Accessed 30th September 2010].

Dashko, N.A. and Yudin, K.B. (1998) Meteorological regime. In: *Hydrometeorology and Hydrochemistry of Seas. Okhotsk Sea, Issue 1: Hydrometeorological Conditions, Part 2*, Vol. IX. Sankt, Petersburg: Hydrometeoizdat Press, pp. 25–75 (in Russian).

Dashko, N.A. and Varlamov, S.M. (2003) Meteorology and climate. In: *Hydrometeorology and Hydrochemistry of Seas. Japan Sea, Issue 1: Hydrometeorological Conditions, Part 2*, Vol. VIII. Sankt, Petersburg: Hydrometeoizdat Press, pp. 18–102 (in Russian).

Dorman, C.E., Enriquez, A.G. and Friehe, C.A. (1995) Structure of the lower atmosphere over the northern California coast during winter. *Monthly Weather Review*, 123, 2384–2404. https://doi.org/10.1175/1520-0493(1995)123%3C2384:SOTLAO%3E2.0.CO;2.

Dorman, C.E., Holt, T., Rogers, D.P. and Edwards, K. (2000) Large-scale structure of the June–July 1996 marine boundary layer along California and Oregon. *Monthly Weather Review*, 128, 1632–1652. https://doi.org/10.1175/1520-0493(2000)128<1632:LSSOTJ>2.0.CO;2.

Dorman, C.E., Beardsley, R.C., Dashko, N.A., Friehe, C.A., Kheilf, D., Cho, K., Limeburner, R. and Varlamov, S.M. (2004) Winter marine atmospheric conditions over the Japan Sea. *Journal of Geophysical Research: Oceans*, 109, C12011. https://doi.org/10.1029/2001JC001197.

Dorman, C.E., Beardsley, R.C., Limeburner, R., Varlamov, S.M., Caruso, M. and Dashko, N.A. (2005) Summer atmospheric conditions over the Japan/East Sea. *Deep-Sea Research II: Topical Studies in Oceanography*, 52, 1393–1420. https://doi.org/10.1016/j.dsr2.2004.09.033.

Dorman, C.E. and Koračin, D. (2008) Response of the summer marine layer with an extreme California coastal bend. *Monthly Weather Review*, 136, 2894–2922. https://doi.org/10.1175/2007MWR2336.1.

Dorman, C.E., Mejia, J. and Koračin, D. (2013) Impact of US west coastline inhomogeneity and synoptic forcing on winds, wind stress and wind stress curl during upwelling season. *Journal of Geophysical Research: Oceans*, 118, 4036–4051. https://doi.org/10.1002/jgrc.20282.

Dorman, C.E., Mejia, J., Koračin, D. and McEvoy, D. (2017) Worldwide marine fog occurrence and climatology. In: Koračin, D. and Dorman, C. (Eds.) *Marine Fog: Challenges and Advancements in Observations, Modeling, and Forecasting. Springer Atmospheric Sciences*. Cham: Springer. https://doi.org/10.1007/978-3-319-45229-6_2.

Dwivedi, S., Narayanan, M.S., Venkat Ratnam, M. and Narayana Rao, D. (2016) Characteristics of monsoon inversions over the Arabian Sea observed by satellite sounder and reanalysis data sets. *Atmospheric Chemistry Physics*, 16, 4497–4509. https://doi.org/10.5194/acp-16-4497-2016.

Earth Systems Laboratory NOAA Niño 3.4 (n.d.) *Nino 3.4, East Central Tropical Pacific SST*. Available at: https://www.esrl.noaa.gov/psd/data/climateindices/list/#TNI [Accessed 15 June 2018].

Earth Systems Research Laboratory NOAA AMO (n.d.) *Atlantic Multidecadal Oscillation Data*. Available at: https://www.esrl.noaa.gov/psd/data/correlation/amon.us.long.data [Accessed 15 June 2018].

Eastman, R., Warren, S.G. and Hahn, C.J. (2011) Variations in cloud cover and cloud types over the ocean from surface observations, 1954–2008. *Journal of Climate*, 24, 5914–5934. https://doi.org/10.1175/2011JCLI3972.1.

Eastman, R., Warren, S.G. and Han, C.J. (2014) *Climatic Atlas of Clouds Over Land and Ocean*. Available at: http://www.atmos.washington.edu/CloudMap/WebO/index.html [Accessed 15 February 2017].

European Marine Observation and Data Network (2016) *EMODnet Digital Bathymetry (DTM)*. Available at: http://doi.org/10.12770/c7b53704-999d-4721-b1a3-04ec60c87238 [Accessed 15 August 2018].

Enfield, D.B. (1981) Thermally driven wind variability in the planetary boundary layer above Lima, Peru. *Journal of Geophysical Research: Oceans*, 86(C3), 2005–2016. https://doi.org/10.1029/JC086iC03p02005.

Enfield, D.B., Mestas-Nunez, A.M. and Trimble, P.J. (2001) The Atlantic multidecadal oscillation and its relationship to rainfall and river flows in the continental U.S. *Geophysical Research Letters*, 28, 2077–2080. https://doi.org/10.1029/2000GL012745.

Filonczuk, M.K., Cayan, D.R. and Riddle, L.G. (1995) *Variability of Marine Fog along the California Coast*. UC San Diego: Scripps Institution of Oceanography. Tech. rep. Available at: http://www.escholarship.org/uc/item/2kc7x97f [Accessed 01 April 2016].

Findlater, J., Roach, W.T. and McHugh, B.C. (1989) The haar of north-East Scotland. *Quarterly Journal of the Royal Meteorological Society*, 115, 581–608. https://doi.org/10.1002/qj.49711548709.

Freeman, E., Woodruff, S.D., Worley, S.J., Lubker, S.J., Kent, E.C., Angel, W.E., et al. (2016) ICOADS release 3.0: a major update to the historical marine climate record. *International Journal of Climatology*, 37, 2211–2332. https://doi.org/10.1002/joc.4775.

Garret, C.I.R. and Loucks, H. (1976) Upwelling along the Yarmouth shore of Nova Scotia. *Journal of the Fisheries Research Board of Canada*, 33, 116–117. https://doi.org/10.1139/f76-013.

Gibbons, J.D. and Chakraborti, S. (2010) *Nonparametric Statistical Inference*. Boca Raton, FL: CRC Press, Chapman & Hall ISBN-13: 978–1420077612.

Guilyardi, E., Wittenberg, A., Fedorov, A., Collins, M., Wang, C., Capotondi, A., van Oldenborgh, G.J. and Stockdale, T. (2009) Understanding El Nino in ocean-atmosphere general circulation models: Progress and challenges. *Bulletin of the American Meteorological Society*, 90, 325–340. https://doi.org/10.1175/2008BAMS2387.1.

Gultepe, I., Tardif, R., Michaelides, S.C., Cermak, J., Bott, A., Bendix, J., Müller, M.D., Pagowski, M., Hansen, B., Ellrod, G., Jacobs, W., Toth, G. and Cober, S.G. (2007) Fog research: a review of past achievements and future perspectives. *Pure Applied Geophysics*, 164, 1121–1159. https://doi.org/10.1007/s00024-007-0211-x.

HadISST (n.d.) *Hadley Centre Sea Ice and Sea Surface Temperature data set (HadISST)*. Available at: https://www.metoffice.gov.uk/hadobs/hadisst/ [Accessed 01 June 2016].

Han, G., Lu, Z., Wang, Z., Helbig, J., Chen, N. and de Young, B. (2008) Seasonal variability of the Labrador current and shelf circulation off Newfoundland. *Journal Geophysical Research: Oceans*, 113(C10013), 1–23. https://doi.org/10.1029/2007JC004376.

Han, G., Ma, Z., deYoung, B., Foreman, M. and Chen, N. (2011) Simulation of three-dimensional circulation and hydrography over the Grand Banks of Newfoundland. *Ocean Modelling*, 40, 199–210. https://doi.org/10.1016/j.ocemod.2011.08.009.

Haraoka, H., Tomine, K., Kawabata, T., Miyamoto, K. and Fukawatase, K. (1995) Some aspects on temperature, humidity and wind profiles in sea fog at Misawa city. *Tenki*, 42, 369–379 Available at: http://jglobal.jst.go.jp/en/public/20090422/200902160222925664 (in Japanese).

Hurrell, J.W. and van Loon, H. (1997) Decadal variations in climate associated with the North Atlantic oscillation. *Climate Change*, 36, 301–326. https://doi.org/10.1023/A:1005314315270.

Hurrell, J.W., Kushnir, Y., Ottersen, G. and Visbeck, M. (2013) An overview of the North Atlantic oscillation. In the North Atlantic oscillation: climate significance and environmental impact, 2013. In: Hurrell, J.W., Kushnir, Y., Ottersen, G. and Visbeck, M. (Eds.) *Geophysical Monograph Series*. Washington, D.C.: American Geophysical Union, p. 134, 279 pp. https://doi.org/10.1029/134GM01.

Isaac, G.A. (2015) *Fog on the Grand Banks*. Available at: https://www.dal.ca/faculty/science/physics/news-events/events-seminars/2015/08/13/fog_on_the_grand_banks.html [Accessed 15 February 2018].

JISAO PDO (n.d.) *The Pacific Decadal Oscillation (PDO)*. Available at: http://research.jisao.washington.edu/pdo/PDO.latest.txt [Accessed 01 June 2016].

Jones, P.D., Jónsson, T. and Wheeler, D. (1997) Extension to the North Atlantic oscillation using early instrumental pressure observations from Gibraltar and south-West Iceland. *International Journal of Climatology*, 17, 1433–1450. https://doi.org/10.1002/(SICI)1097-0088(19971115)17:13<1433::AID-JOC203>3.0.CO;2-P.

Jury, M.R. (1985) Case studies of alongshore variations in wind driven upwelling in the southern Benguela region. South African Ocean color and upwelling experiment. In: Shannon, L.V. (Ed.) *Sea Fisheries Research Institute, University of Cape Town, Cape Town, South Africa*. pp. 29–46 ISBN 9780621073867.

Karoly, D.J. and Vincent, D.G. (1998) Meteorology of the southern hemisphere. *Meteorological Monographs*, 49, 1–410. https://doi.org/10.1175/0065-9401-27.49.1.

Kim, C.K. and Yum, S.S. (2010) Local meteorological and synoptic characteristics of fogs formed over Incheon international airport in the west coast of Korea advances in atmospheric. *Sciences*, 27, 761–776. https://doi.org/10.1007/s00376-009-9090-7.

Knight, J.R., Folland, C.K. and Scaife, A.A. (2006) Climate impacts of the Atlantic multidecadal oscillation. *Geophysical Research Letters*, 33, L17706. https://doi.org/10.1029/2006GL026242.

Koračin, D., Dorman, C.E. and Dever, E.P. (2004) Coastal perturbations of marine-layer winds, wind stress, and wind stress curl along California and Baja California in June 1999. *Journal of Physical Oceanography*, 34, 1152–1173. https://doi.org/10.1175/1520-0485(2004)034<1152:CPOMWW>2.0.CO;2.

Koračin, D., Dorman, C.E., Lewis, J.M., Hudson, J.G., Wilcox, E.M. and Torregrosa, A. (2014) Marine fog: a review. *Atmospheric Research*, 143, 142–175. https://doi.org/10.1016/j.atmosres.12.012.

Koračin, D. and Dorman, C. (Eds.). (2017) *Marine Fog: Challenges and Advancements in Observations, Modeling, and Forecasting*. Springer Atmospheric Sciences, Switzerland: Springer International Publishing, p. 537. https://doi.org/10.1007/978-3-319-45229-6.

Lewis, J.M., Koračin, D. and Redmond, K.T. (2004) Sea fog research in the United Kingdom and United States: a historical essay including outlook. *Bulletin of the American Meteorological Society*, 85, 395–408. https://doi.org/10.1175/BAMS-85-3-395.

Leipper, D.F. (1994) Fog on the U.S. west coast: a review. *Bulletin of the American Meteorological Society*, 75, 229–240. https://doi.org/10.1175/1520-0477(1994)075<0229:FOTUWC>2.0.CO;2.

Mantua, N.J., Hare, S.R., Zhang, Y., Wallace, J.M. and Francis, R.C. (1997) A Pacific interdecadal climate oscillation with impacts on salmon production. *Bulletin of the American Meteorological Society*, 78, 1069–1079. https://doi.org/10.1175/1520-0477(1997)078,1069:APICOW.2.0.CO;2.

Mesias, J.M., Bisagni, J.J. and Brunner, A.-M.E.G. (2007) A high-resolution satellite-derived sea surface temperature climatology for the western North Atlantic Ocean. *Continental Shelf Research*, 27, 191–207. https://doi.org/10.1016/j.csr.2006.10.002.

Myers, J.L. and Well, A.D. (2003) *Research Design and Statistical Analysis*, 3rd edition. Mahwah, N.J: Lawrence Erlbaum, p. 508 ISBN-10: 0805864318.

Newman, M., Alexander, M.A., Ault, T.R., Cobb, K.M., Deser, C., Di Lorenzo, E., et al. (2016) The Pacific decadal oscillation, revisited. *Journal of Climate*, 29, 4399–4427. https://doi.org/10.1175/JCLI-D-15-0508.1.

National Centers for Environmental Information NOAA (n.d.) Temperature. Available at: https://www.nodc.noaa.gov/cgi-bin/OC5/SELECT/woaselect.pl [Accessed dd mmm yyyy].

Norris, J.R. (1999) On trends and possible artifacts in global ocean cloud cover between 1952 and 1995. *Journal of Climate*, 12, 1864–1870.

O'Reilly, C.H., Woollings, T. and Zanna, L. (2017) The dynamical influence of the Atlantic multidecadal oscillation on continental climate. *Journal of Climate*, 30, 7213–7230. https://doi.org/10.1175/JCLI-D-16-0345.1.

Ramage, C.S. (1971) *Monsoon Meteorology*. New York, NY: Academic Press ISBN 0125766505.

Rayner, N.A., Parker, D.E., Horton, E.B., Folland, C.K., Alexander, L.V., Rowell, D.P., et al. (2003) Global analyses of sea surface temperature, sea ice, and night marine air temperature since the late nineteenth century. *Journal of Geophysical Research: Atmospheres*, 108(D14), 4407. https://doi.org/10.1029/2002JD002670.

Schemenauer, R.S., Fuenzalida, H. and Cereceda, H.P. (1988) A neglected water resource: the Camanchaca of South America. *Bulletin of the American Meteorological Society*, 69, 138–147. https://doi.org/10.1175/1520-0477(1988)069<0138:ANWRTC>2.0.CO;2.

Seifert, T., Tauber, F. and Kayser, B. (2001) *A High Resolution Spherical Grid Topography of the Baltic Sea*, 2nd edition. Stockholm: Baltic Sea Science Congress, Poster #147, www.io-warnemuende.de/iowtopo. Available at: https://www.io-warnemuende.de/topography-of-the-baltic-sea-data-compilation.html [Accessed November 2001].

Serreze, M.C., Carse, F., Barry, R.G. and Rogers, J.C. (1997) Icelandic low cyclone activity: climatological features, linkages with the NAO and relationships with recent changes in the northern hemisphere circulation. *Journal of Climate*, 10, 453–464. https://doi.org/10.1175/1520-0442(1997)010<0453:ILCACF>2.0.CO;2.

Schott, F.A. and McCreary, J.P., Jr. (2001) The monsoon circulation of the Indian Ocean. *Progress in Oceanography*, 51, 1–123. https://doi.org/10.1016/S0079-6611(01)00083-0.

Smith, R.L. (1968) Upwelling. *Oceanography and Marine Biology An Annual Review*, 6, 11–46 Available at: http://asas.drupia.com/oceanography-and-marine-biology-an-annual-review-vol-6.pdf.

Smith, C.A. and Sardeshmukh, P.D. (2000) The effect of ENSO on the intraseasonal variance of surface temperature in winter. *International Journal of Climatology*, 20, 1543–1557. https://doi.org/10.1002/1097-0088(20001115)20:13<1543::AID-JOC579>3.0.CO;2-A.

Stephenson, D.B., Wanner, H., Brönnimann, S. and Luterbacher, J. (2003) The history of scientific research on the North Atlantic oscillation. In: Hurrell, J.W., Kushnir, Y., Ottersen, G. and Visbeck, M. (Eds.) *The North Atlantic Oscillation: Climatic Significance and Environmental Impact*. Washington, DC: American Geophysical Union, pp. 37–50. https://doi.org/10.1029/134GM02.

Stuart, D.W. and Wirfel, W.P. (1980) *Aircraft soundings along coastal Peru during Joint II 1976. FSU-MET-STU 80-5*. Tallahassee, FL: Department of Meteorology, Florida State University. 100 pp.

Sugimoto, S., Sato, T. and Nakamura, K. (2013) Effects of synoptic-scale control on long-term declining trends of summer fog frequency over the Pacific side of Hokkaido Island. *Journal of Applied Meteorology and Climatology*, 52, 2226–2242. https://doi.org/10.1175/JAMC-D-12-0192.1.

Taljaard, J.J. (1972) Synoptic meteorology of the southern hemisphere. In: Newton, C.W. (Ed.) *Meteorology of the Southern Hemisphere. Meteorological Monographs*, Vol. 13. Boston, MA: American Meteorological Society. https://doi.org/10.1007/978-1-935704-33-1_8.

Taylor, G.I. (1917) The formation of fog and mist. *Quarterly Journal of the Royal Meteorological Society*, 43, 241–268. https://doi.org/10.1002/qj.49704318302.

Tokinaga, H. and Xie, S.-P. (2009) Ocean tidal cooling effect on summer sea fog over the Okhotsk Sea. *Journal of Geophysical Research: Atmospheres*, 114, D14102. https://doi.org/10.1029/2008JD011477.

Tomczak, M. and Godfrey, J.S. (2003) *Regional Oceanography: An Introduction*. ISBN: 8170353068. Retrieved from http://www.es.flinders.edu.au/~mattom/regoc/pdfversion.html [Accessed dd mmm yyyy].

Torregrosa, A., Combs, C. and Peters, J. (2016) GOES-derived fog and low cloud indices for coastal north and Central California ecological analyses. *Earth and Space Science*, 3, 46–67. https://doi.org/10.1002/2015EA000119.

Townsend, D.W., Thomas, A.C., Mayer, L.M., Thomas, M.A. and Quinlan, J.A. (2006) Oceanography of the Northwest Atlantic continental shelf. In: Robinson, A.R. and Brink, K.H. (Eds.) *The Sea, Ideas and Observations on Progress in the Study of the Seas*, Vol. 14A. Cambridge, MA: Harvard University Press, pp. 119–168 ISBN 9780674015272.

Trenberth, K., Zhang, R. and National Center for Atmospheric Research Staff (Eds.). (2017) The Climate Data Guide: Atlantic Multi-decadal Oscillation (AMO). Available at: https://climatedataguide.ucar.edu/climate-data/atlantic-multi-decadal-oscillation-amo [Accessed dd mmm yyyy].

U.S. Department of Agriculture (1938) Atlas of the Climatic Charts of the Oceans. Publication No. 1247. *Prepared under the supervision of W. F. McDonald, 130 charts. U.S. Weather Bureau.* Available at: ftp://ftp.nodc.noaa.gov/pub/data.nodc/woa/PUBLICATIONS/english58.pdf

Valla, D. and Piola, A.R. (2015) Evidence of upwelling events at the northern Patagonian shelf break. *Journal of Geophysical Research: Oceans*, 120, 7635–7656. https://doi.org/10.1002/2015JC011002.

van Loon, H. (1984) Climates of the oceans. World survey of climatology. In: *World Survey of Climatology, Editor-in-Chief H. E. Landsberg*, Vol. 15. Amsterdam, Netherlands: Elsevier, pp. 453–458. https://doi.org/10.1002/joc.3370050110.

von Ficker, H. (1936) *Die Passatinversion. Veröffentlichungen des Meteorologischen Instituts der Universität Berlin*. Berlin: Dietrich Reimer Vlg.

Wang, B. (Ed.). (1985) *Sea Fog*. Beijing: China Ocean Press. https://doi.org/10.1016/0377-0265(87)90018-2.

Wang, X.L. (2006) Climatology and trends in some adverse and fair weather conditions in Canada, 1953–2004. *Journal of Geophysical Research: Atmospheres*, 111, D09105. https://doi.org/10.1029/2005JD006155.

Wang, S., Huang, J., He, Y. and Guan, Y. (2014) Combined effects of the Pacific decadal oscillation and El Niño–Southern Oscillation on global land dry–wet changes. *Scientific Reports*, 4, 6651. https://doi.org/10.1038/srep06651.

WMO (2009) *WMO-No. 306, Manual on Codes*. International Codes, vol. I.1. Available at: http://marswiki.jrc.ec.europa.eu/agri4castwiki/images/a/ad/WMO_306_VolI1_en.pdf [Accessed 1 September 2015].

Woodruff, S.D., Slutz, R.J., Jenne, R.L. and Steurer, P.M. (1987) A comprehensive ocean-atmosphere data set. *Bulletin of the American Meteorological Society*, 68, 1239–1250. https://doi.org/10.1175/1520-0477(1987)068<1239:ACOADS>2.0.CO;2.

Worley, S.J., Woodruff, S.D., Reynolds, R.W., Lubker, S.J. and Lott, N. (2005) ICOADS release 2.1 data and products. *International Journal of Climatology*, 25, 823–842. https://doi.org/10.1002/joc.1166.

Zhang, S.-P., Xie, S.-P., Liu, Q.-L., Yang, Y.-Q., Wang, X.-G. and Ren, Z.-P. (2009) Seasonal variations of Yellow Sea fog: observations and mechanisms. *Journal of Climate*, 22, 6758–6772. https://dx.doi.org/10.1175/2009JCLI2806.1.